The Astrophysical Journal Supplement Series, 217:3 (29pp), 2015 March doi:10.1088/0067-0049/217/1/3

O I AND Ca II OBSERVATIONS IN INTERMEDIATE REDSHIFT QUASARS*

Mary Loli Martínez-Aldama[1], Deborah Dultzin[1], Paola Marziani[2], Jack W. Sulentic[3], Alessandro Bressan[4], Yang Chen[4], and Giovanna M. Stirpe[5]
[1] Instituto de Astronomía, Universidad Nacional Autónoma de México, México
[2] INAF, Osservatorio Astronomico di Padova, Italia
[3] IAA-CSIC, Granada, España
[4] Scuola Internazionale Superiore di Studi Avanzati (SISSA), Trieste, Italy
[5] INAF, Osservatorio Astronomico di Bologna, Italy
Received 2014 May 30; accepted 2015 January 5; published 2015 February 26

ABSTRACT

We present an unprecedented spectroscopic survey of the Ca II triplet + O I for a sample of 14 luminous ($-26 \gtrsim M_V \gtrsim -29$), intermediate redshift ($0.85 \lesssim z \lesssim 1.65$) quasars. The Infrared Spectrometer and Array Camera spectrometer on the ESO Very Large Telescope allowed us to cover the Ca II near-infrared spectral region redshifted into the *H* and *K* windows. We describe in detail our data analysis which enabled us to detect Ca II triplet emission in all 14 sources (with the possible exception of HE0048–2804) and to retrieve accurate line widths and fluxes of the triplet and O I λ8446. The new measurements show trends consistent with previous lower-*z* observations, indicating that Ca II and optical Fe II emission are probably closely related. The ratio between the Ca II triplet and the optical Fe II blend at λ4570 Å is apparently systematically larger in our intermediate redshift sample relative to a low-*z* control sample. Even if this result needs a larger sample for adequate interpretation, higher Ca II/optical Fe II should be associated with recent episodes of star formation in intermediate redshift quasars and, at least in part, explain the apparent correlation of Ca II triplet equivalent width with *z* and *L*. The Ca II triplet measures yield significant constraints on the emitting region density and ionization parameter, implying Ca II triplet emission from $\log n_{\rm H} \gtrsim 11$ [cm^{-3}] and ionization parameter $\log U \lesssim -1.5$. The line width and intensity ratios suggest properties consistent with emission from the outer part of a high-density broad line region (a line emitting accretion disk?).

Key words: black hole physics – line: profiles – quasars: emission lines – quasars: general

1. INTRODUCTION

Explaining the origin of Fe emission in quasar spectra is a long-standing problem in studies of active galactic nuclei (AGNs). Recent observations and models fail to reach a consensus on the ionization mechanism, even in the case of moderate Fe II emitters. Purely collisional models are unable to account for the spectral energy distribution of Fe II emitters (Kuehn et al. 2008). At the same time, the ratio of UV Fe II to optical Fe II emission is more easily explained in the context of collisional ionization (Sameshima et al. 2011). Akn 564 Fe II reverberates in response to continuum changes (Shapovalova et al. 2012), providing support for the role of photoionization. At the same time, Akn 120 Fe II does not show any response (Kuehn et al. 2008). The extreme complexity of the Fe II ion makes theoretical model calculations very difficult and line blending makes estimation of the Fe II width and strength parameters uncertain.

Given the difficulty involved with the interpretation and prediction of the Fe II spectrum, the study of simpler ionic species like Ca II (emitting the IR triplet λ8498, λ8542, λ8662, hereafter CaT) and O I is more straightforward. The Ca II ion is much simpler. The ionization potential of neutral Calcium ($\approx$6.1 eV) leads us to expect that Ca II ions exist where Hydrogen is not fully ionized. Several lines of evidence suggest that CaT and optical Fe II are produced in the same region. Data from Persson (1988) and photoionization calculations (Joly 1989) found that CaT is emitted by gas at low temperature (8000 K), high density (>10^{11} cm^{-3}), and high column density (>10^{23} cm^{-2}), similar to optical Fe II. Matsuoka et al. (2007, 2008) computed photoionization models using the O I λ8446 and λ11287 lines and CaT, and found that a high density ($\sim 10^{11.5}$ cm^{-3}) and low ionization parameter ($U \sim 10^{-2.5}$) are needed to reproduce flux ratios consistent with the physical conditions expected for optical Fe II emission. The density and ionization parameters are in agreement with those found by Joly (1989).

Ferland & Persson (1989) improved the photoionization models by including physical processes like H^0 free–free, H^- bound-free, and Compton recoil ionization. These authors demonstrated the need for very large column densities ($N_c > 10^{24.5}$ cm^{-2}) to reproduce the Ca II spectrum. Such large column densities could be provided by an accretion disk. A similar behavior to the one described by Joly (1989) for CaT/Hβ and Fe II/Hβ was found by Dultzin-Hacyan et al. (1999). These authors also suggested that the line emitting region could be associated with the outer part of an accretion disk. The width measured for the unblended Fe II λ 11126 line (which belongs to the so-called 1μm Fe II lines) is very similar to those of CaT and O I λ8446 and narrower than that of the Hydrogen lines. In a purely kinematical interpretation, this means that low ionization lines like Fe II, CaT, and O I λ8446 are emitted in the outer zone of the broad line region (BLR; Rodríguez-Ardila et al. 2002a, 2002b; Matsuoka et al. 2007, 2008), and are probably associated with the accretion disk with physical conditions different from the region emitting most of the high ionization lines.

* Based on observations collected at the European Organization for Astronomical Research in the southern hemisphere, Chile, under programme ID 085.B-0158(A).

Physical modeling (via a photoionization code like CLOUDY, Ferland et al. 2013) requires input from measurements that are retrieved through model fits of the observed spectra. The Ca II triplet and O I λ8446 lines can be easier to model than Fe II but they are not as strong as Fe II optical features which, however, are heavily blended. They are located in a wavelength range where the putative accretion disk continuum and the high-energy tail of hot dust emission form a sort of valley in the spectral energy distribution. The old stellar population associated with the quasar host galaxy peaks at $\approx$1 μm (Landt et al. 2011). In many low-luminosity quasars, CaT and O I λ8446 are confused with the underlying absorption of the host galaxy.

The near-infrared region (NIR) has not been easy to observe due to the lack of high-quality IR spectrometers. Only in relatively recent times has the development of new instruments made it possible to obtain high signal-to-noise ratio (S/N) spectra for sources with redshifts larger than $z \gtrsim 0.1$. It is not surprising that the Ca II and O I features remain relatively unstudied even in sources for which a wealth of optical data exists.

The present work extends the study of the Ca II triplet in emission to include 14 high-luminosity and intermediate-redshift quasars (Section 2). Whenever possible, they are analyzed within the 4D eigenvector 1 context (4DE1; Boroson & Green 1992; Sulentic et al. 2000a, 2000b, 2007; Marziani et al. 2001, 2003a, 2003b), which serves as a spectroscopic unifier/discriminator of the emission line properties for type 1 AGNs. The parameters defining the four dimensions of the E1 space involve: (1) FWHM(H$\beta_{\rm BC}$), (2) the ratio between the equivalent width (W) of the optical Fe II λ 4570 blend and Hβ, $R_{\rm Fe\,II} = W({\rm Fe\,II}\ \lambda4570)/W({\rm H}\beta) \approx I({\rm Fe\,II}\ \lambda4570)/I({\rm H}\beta)$, (3) the soft X-ray photon index ($\Gamma_{\rm soft}$), and (4) the centroid line shift of high-ionization C IV λ1549, with the strongest correlations involving parameters 2–4 (Sulentic et al. 2007). In the 4DE1 framework, broad line AGNs can be divided into two populations, A and B (Sulentic et al. 2002). Considering the broad component (BC) of the Hβ line, populations A and B can be separated at FWHM(H$\beta_{\rm BC}$) = 4000 km s^{-1}. The spectra of sources above and below this limit look substantially different. It is possible to introduce a finer subdivision that will not be used in this paper because of its small sample size: we will distinguish sources as Pop. A or B only. Quasars can be divided into bins of ΔFWHM(Hβ) and $\Delta R_{\rm Fe\,II}$. The bins of Pop. A (A1, A2, A3, A4) are defined in terms of increasing $R_{\rm Fe\,II}$, while Pop. B bins (B1, B1^{+}, B1^{++}) are defined in terms of increasing FWHM(Hβ). Population A shows (1) a scarcity of RL sources, (2) strong/moderate Fe II emission, (3) a soft X-ray excess, (4) high-ionization broad lines (HIL) with blueshift/asymmetry, and (5) low-ionization broad line profiles (LIL) best described by Lorentz fits. Population B (1) includes the large majority of RL sources, (2) shows weak/moderate Fe II emission, and (3) includes sources with less prominent or no soft X-ray excess (Sulentic et al. 2007) and (4) with HIL blueshift/asymmetry or no blue shifts at all. Finally, (5) Pop. B shows LIL Balmer lines best fit with double Gaussian models. The physical drivers that change along the 4DE1 sequence have been identified: number density appears to increase from Pop. B to A, and black hole mass increases with large scatter from A to B. The principal driver of source occupation in 4DE1 space is probably the Eddington ratio, which increases from B to A (Marziani et al. 2001; Boroson 2002). The 4DE1 parameter space is, to first approximation, not strongly dependent on luminosity. The same basic distinction between Pop. A and B is also recognizable for very luminous sources (Marziani et al. 2009).

This paper presents new observations and data reduction of the spectra of the Ca II IR triplet, as a representative LIL, as well as of the O I λ8446 line in very luminous quasars of the Hamburg-ESO (HE) survey (Sections 2–4). We discuss in some detail the identified line and continuum components for a proper data analysis (Section 5). The basic results obtained from the measurements are briefly reported in Section 6. In Section 7, we compare observational data and photoionization predictions, the role of CaT and O I λ8446 within the 4DE1 context, possible implications for star formation, and a preliminary geometry for the BLR. Conclusions are presented in Section 8.

2. SAMPLE SELECTION

Our original sample of HE sources was defined with the aim of testing/extending the 4DE1 correlation at relatively high z and at high luminosity (Marziani et al. 2009). The HE original sample of Hβ Infrared Spectrometer and Array Camera (ISAAC) observations was therefore flux limited and unbiased in terms of Fe II strength. Our Ca II subsample was extracted from the 52 source ISAAC sample of Marziani et al. (2009). The only selection criterion was that IR atmospheric absorptions did not affect the Ca II and O I lines. All of the targets in the present investigation therefore have optical spectra around Hβ already obtained with the same instrument.

The Ca II + O I sample contains 15 high-luminosity HE quasars with M_B <–26 in the redshift range $0.846 < z < 1.638$. They were observed using the Very Large Telescope (VLT-UT3) equipped with ISAAC which yielded a spectral resolution of $R_S \approx 1000$. Sample characteristics and the log of the observations are reported in Table 1. The first column lists the coordinate name from the HE survey for each object of our sample. In columns 2–5, we report redshift, apparent and absolute magnitudes, and Kellerman's radio-loudness parameter, as previously given by Sulentic et al. (2004) and Marziani et al. (2009). Column 6 lists the population in the Eigenvector 1 sequence (Sulentic et al. 2002). One of the sources (HE2259–5524) was excluded from the analysis because of poor S/N.

The median absolute magnitude of the selected 14 HE sources is $\approx$–28, which makes them among the most luminous quasars known. The sample presented in this paper is small; however, Ca II and O I observations of quasars until now have been obtained for only 66 sources (Persson 1988; Matsuoka et al. 2005, 2007, 2008; Landt et al. 2008), of which only 1 is at $z > 1$. Therefore, the present sample represents the first systematic study of the Ca II and O I lines in quasars at redshift > 1.

In the following, we will consider as a reference low-z, low-luminosity "control" sample the sources of Persson (1988) which were observed with very high S/N and spectral resolution, similar to the one achieved in the present paper. This previous Ca II sample contained sources with strong Fe II emission at low redshift, similar to other, more recent samples (Matsuoka et al. 2007). We stress again that our sample is not selected on the basis of Fe II intensity. The selected ISAAC sources do not show very strong optical Fe II emission: 10 of them are Pop. B and 4 are Pop. A

Table 1
Basic Properties of Sources and Log of Observations

Object[a]	z[b]	m_B^c	M_B^d	log R_K^e	Population[f]	Date[g]	Band[h]	DIT[i]	N_{exp}^j	Seeing[k]	S/N[l]
HE0005–2355	1.4120	16.9	−27.6	2.56	B1	07/30/10	*K*	120	6	1.054	20
HE0035–2853	1.6377	17.0	−28.1	<0.21	B2	07/27/10	*K*	150	4	0.840	55
HE0043–2300	1.5402	17.1	−27.9	2.03	A1	07/07/10	*K*	120	6	1.078	45
HE0048–2804	0.8467	17.3	−26.0	···	B1	07/27/10	*H*	150	8	0.863	35
HE0058–3231	1.5821	17.1	−27.9	<0.24	B1	07/27/10	*K*	150	4	0.759	10
HE0203–4627	1.4381	17.3	−27.5	2.07	B1	07/02/10	*K*	180	6	1.184	25
HE0248–3628	1.5355	16.6	−28.2	0.55	A1	07/22/10	*K*	120	6	0.965	50
HE1349+0007	1.4442	16.8	−28.0	−0.18	B1	04/15/10	*K*	150	6	0.749	20
HE1409+0101	1.6497	16.9	−28.3	0.4	B1	04/15/10	*K*	150	6	0.775	25
HE2147–3212	1.5432	16.8	−28.2	<0.14	B2	06/12/10	*K*	120	6	0.847	20
HE2202–2557	1.5347	16.7	−28.1	1.8	B1	07/23/10	*K*	120	6	0.606	40
HE2259–5524	0.8549	17.1	−26.1	···	A2	05/25/10	*H*	150	8	1.863	10
HE2340–4443	0.9216	17.1	−26.3	···	A1	07/23/10	*H*	120	6	0.568	25
HE2349–3800	1.6040	17.5	−27.4	1.93	B1	06/12/10	*K*	120	6	0.789	20
HE2352–4010	1.5799	16.1	−28.8	···	A1	07/23/10	*K*	150	6	0.639	35

[a] Hamburg/ESO Survey coordinate name.
[b] Heliocentric redshift.
[c] Apparent Johnson *B* magnitude
[d] Absolute *B* magnitude.
[e] Decimal logarithm of the ratio between specific flux at 6 cm and 4440 Å. References for redshift uncertainty, apparent, absolute magnitude, and ratio radio to optical: (1) Sulentic et al. (2004); (2) Marziani et al. (2009).
[f] Spectral type according to the Eigenvector 1 scheme (Sulentic et al. 2002).
[g] Date of observation.
[h] Photometric band of the covered spectra range.
[i] Detector Integration Time (DIT) in seconds.
[j] Number of exposures with a single exposure time equal to DIT.
[k] Average seeing.
[l] S/N (1σ) at continuum level.

(Table 1). The Pop. A sources are of spectral type A1 following Sulentic et al. (2002), and for all sources we therefore have $R_{\rm Fe\,II} \lesssim 0.5$. This allows us to explore a domain in the Fe II emission and in the 4DE1 parameter space where the study of Ca II could provide new insights into the origin of low-ionization lines for the majority of quasars with moderate Fe II emission. At the same time, the preferential selection of high $R_{\rm Fe\,II}$ sources at low-*z* should be taken into account when possible luminosity and *z* effects are studied.

3. OBSERVATIONS

Observations aimed to obtain spectra of the O I λ8446 and CaT lines for the sample described in the previous section. Considering the rather low efficiency of IR spectrometers available until a few years ago and the relatively low equivalent width of the features we wanted to observe (≈10–20 Å), the collecting area of a large telescope was needed to obtain a sufficient signal with moderate dispersion.

The VLT includes four 8.2 m diameter telescopes located on top of Cerro Paranal, and instruments are mounted at the foci of the four telescopes. ISAAC was[6] one of them, and for many years has been one of the few instruments available worldwide for moderate-resolution IR spectroscopy of faint sources like high-*z* quasars. ISAAC was able to obtain images and spectra in the wavelength range 1–5 μm (Moorwood et al. 1998). It was equipped with gratings for high ($R_S \sim 3000$) and low spectral resolution ($R_S \sim 1000$).

Our spectra were collected on the Rockwell CCD detector (pixel size 18.5 μm yielding a pixel scale of 0.″148/pixel) at low resolution but with a slit width of 0.″6, that ensured $R_S \approx 1000$, as measured on sky and arc lamp lines. The second part of Table 1 provides the date of observation, the photometric band of the covered ranges, the detector integration time (DIT), and the number of sequential exposures with fixed DIT in the spectral band covering the CaT + O I blend. Seeing values, reported in the penultimate column of Table 1, are averages over 10–15 measures at Paranal obtained during each quasar exposure. The S/N was measured on the continuum at 8300–8400 Å. The instrumental spectral resolution at FWHM measured on sky lines was ≈330 km s^{-1}.

4. DATA REDUCTION

We used the IRAF software to reduce our spectra. Frames were obtained alternating exposures of two or three DITs in two different positions (A and B) along the slit, following an A–B–B–A sequence. The frames in each position were averaged and then subtracted one from the other. This procedure cancelled the bias and dark current present on each frame, assuming that they remained constant during the sequence, and also subtracted most of the sky background, facilitating the spectrum extraction. After subtraction, the frames were divided by the corresponding flat fields. We extracted the 1D spectra using the IRAF task APSUM where a low-order polynomial function was fitted and subtracted to eliminate any residual background. 1D spectra were wavelength calibrated using an Ar–Xe lamp. The calibration was achieved using a third-order polynomial with a typical rms of 0.3 Å in the *H* band and 0.4 Å in the *K* band. This calibration, if applied to the sky spectrum, yielded a slight displacement that was corrected using measures of OH sky line wavelengths. We

[6] ISAAC was decommissioned in 2013.

applied the offset-corrected wavelength calibration to the quasar spectra. Finally, 1D quasar spectra were combined to obtain one median spectrum. The spectra of the standard stars (observed right before or after the quasar spectrum) were extracted and wavelength calibrated in the same way.

We corrected for the effect of telluric lines using the TELLURIC IRAF task. This procedure involved a change in the quasar continuum shape since the task TELLURIC carried out a division between the quasar and the standard star. To return to the original quasar continuum after the elimination of the telluric bands, we divided the quasar spectrum by the standard star continuum (i.e., by the standard star divided by a synthetic atmospheric transmission spectrum).

Fourteen standard stars were spectral type B and one was spectral type G. The B stars belonged to different luminosity classes (supergiants, giants, and main sequence), while the G star is a main-sequence star. Comparing the NIR stellar spectral library from Ranade et al. (2004) and Ranade et al. (2007) with theoretical libraries in the H and K bands (Pickles 1998), we found that the theoretical spectra could reproduce the observed spectra of main-sequence stars but not those of giants and supergiant stars. For the giant and supergiant stars, we considered a spectral energy distribution provided by blackbody emission at the temperature tabulated for the star (Ammons et al. 2006). Blackbody emission fits the spectra very well after erasing the stellar absorptions lines with the tool XYDRAW of the SPLOT IRAF task (see Figure 1). In order to render our approach uniform, we fitted all of the stars using a blackbody because there is practically no difference between the simple blackbody fit and the continuum spectra of the stars. Finally, the standard star spectra were normalized to H and K 2MASS magnitudes.

The sensitivity function was obtained by dividing the standard star spectra by the blackbody model. The final relative flux calibration was achieved by dividing the spectrum by the sensitivity function. Spectra were corrected for Galactic extinction following Schlegel et al. (1998) but no internal extinction correction was applied. Quasar spectra were normalized to 2MASS magnitudes as was done for the standard stars in order to minimize the effect in the continuum flux change possibly induced by intrinsic variability (see next section). Redshift correction was performed using the redshift values reported in Sulentic et al. (2004) and Marziani et al. (2009). These redshifts were measured on $H\beta_{NC}$, $H\gamma_{NC}$ and [O III] $\lambda\lambda$4959, 5007 with an uncertainty usually $cz < 150$ km s^{-1} in the rest frame. Figure 2 shows the rest-frame flux and wavelength-calibrated spectra before continuum subtraction.

4.1. Variability

The Hβ spectra were taken between 2001 and 2005, while the NIR spectra were collected in 2010. There is a difference of 5–10 yr between the Hβ and NIR observations. In order to estimate a possible broad line flux variation in response to continuum changes, we used the BLR radius versus luminosity relation of Bentz et al. (2013). Comparing the expected response time with the difference in date between the optical and IR observations, we found that eight objects could have varied. Extracting the light curves from the Catalina Real-Time Transient Survey (CRTS; Drake et al. 2009), we could identify eight cases of actual variation. Five of the eight objects show a systematic variation $\lesssim$0.1 mag in a period of 6–8 yr when they were monitored by CRTS. The remaining three objects, HE0048–2804, HE0203–4627, and HE2147–3212, show a "high frequency" variation which is apparent even from visual inspection of the light curve. The amplitude is modest, $\approx$0.2 mag, and does not hint at any systematic variation over longer periods. We normalized the Ca II spectra to H and K 2MASS magnitudes, and the Hβ spectra to J and H magnitudes, in order to obtain an accurate flux scale as well as to remove any variability effect on line and continuum fluxes. This normalization was not possible for two objects, HE0048–2804 and HE2340–4443, since 2MASS does not have information on the I or Z photometric bands that cover redshifted Hβ (see Appendix A for a brief discussion).

5. MEASUREMENTS

The fits and data analysis were carried out within the Eigenvector 1 context (Boroson & Green 1992; Sulentic et al. 2000a, 2000b, 2007; Marziani et al. 2001, 2003a, 2003b). We performed multicomponent fits including all of the relevant components that we presume contribute to the spectral ranges under investigation. The objects analyzed in this paper belong to a sample of intermediate redshift quasars for which Hβ is available from previous ISAAC observations. The Hβ line profile parameters can guide us in the interpretation of the NIR region. The optical spectra were previously analyzed by Sulentic et al. (2004) and Marziani et al. (2009). The analysis of this paper adds an Hβ multicomponent SPECFIT modeling that was not carried out for individual sources or, if carried out, was not presented in previous papers. The optical and the NIR spectra were modeled with the task SPECFIT of IRAF, a routine that carries out simultaneous fits of several line and continuum components to 1D spectra (Kriss 1994). Each component is described by a set of parameters that are varied according to the initial guess between a maximum and a minimum value. The best fit is achieved via χ^2 minimization. The multicomponents fits are shown in the Figure 3. The left panel shows the optical spectra and the right panel the NIR spectra.

Few parameters were actually free to vary in the NIR spectral range. The Hβ profile was taken as a proxy for Pa9 λ9229 and O I λ8446, and the peak shifts of these two lines were set as measured on Hβ. The flux ratio between the BC and the very broad component (VBC) of Pa9 is assumed to be the same for Hβ. The width and shift of [O III] $\lambda\lambda$4959, 5007 set the width and shift of [S III] λ9531, so that only the intensity of the latter line is left free to vary. The centroid of CaT was set in the quasar rest-frame. The only remaining free parameters were therefore the specific flux scale and the index of the power-law continuum (2), the intensity scaling of the Fe II template (2), the intensity and width of O I λ8446 and CaT (4), the intensity scaling of the high-order Paschen lines (1), and the intensity and temperature of Paschen continuum (PaC) (2), providing a total number of 11 free parameters. However, not all of these parameters refer to features blended with O I λ8446 and CaT: the PaC properties do not affect the blend O I + CaT; the intensity scalings of the high-order Paschen lines and of the Fe II template are also set by features outside of the blend. This makes the fits more robust, and ensures that O I λ8446 + CaT intensity and width are the parameters most affecting the χ^2_ν in the wavelength range they cover. The following sections describe each one of the components used for the fits and the error estimates.

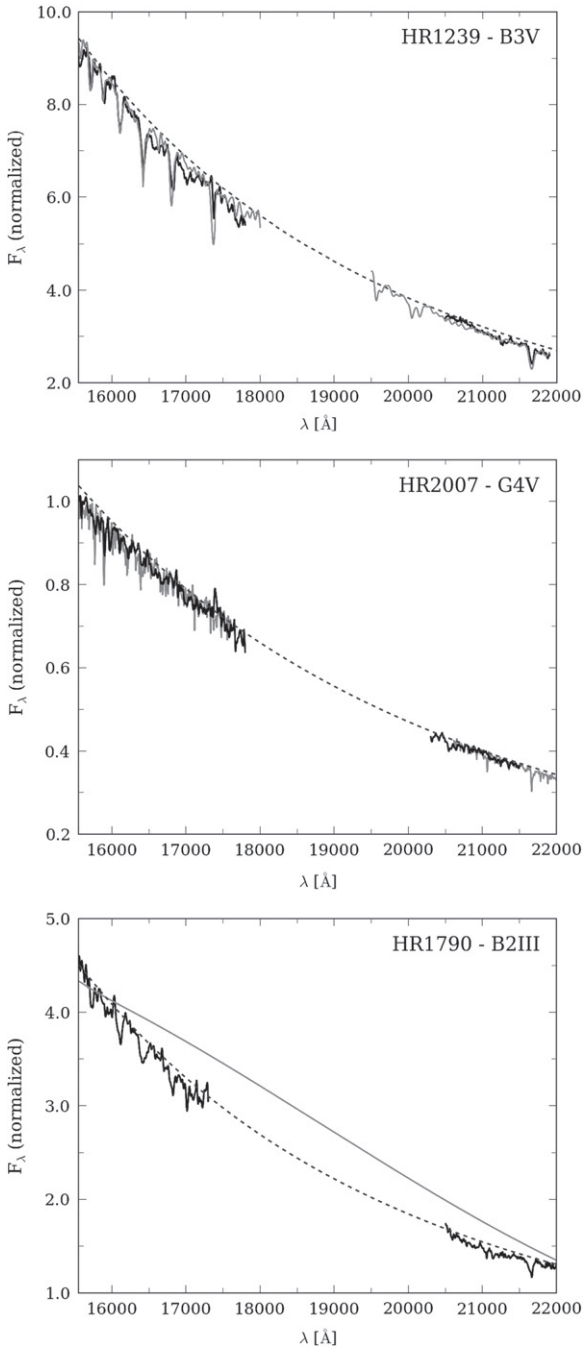

Figure 1. Comparison between Pickles stellar theoretical and observed emission of main-sequence B (upper panel) and G (middle panel) stars and a giant B (bottom panel) star with a blackbody spectral energy distribution. The black line is the observed emission, the gray line is the theoretical emission, and the dashed line is the blackbody emission.

5.1. Continuum

The main continuum emission present in the UV to NIR spectral region of quasars is due to an accretion disk (Malkan & Sargent 1982; Malkan 1983). Accretion disk emission is thermal (a "stretched blackbody") but can be modeled locally with a power law with a slope of −2.4. Optical and NIR spectra should share in part the same underlying continuum, i.e., the low-energy tail of the accretion disk emission. However, we could not consistently fit the continuum with a single slope from the optical to the NIR. In the majority of sources, the NIR spectrum is ∼30–80% above the NIR extrapolation of the optical continuum. Therefore, a local power-law continuum was fit for each quasar assuming a free power-law index. The optical continuum was defined at 4750 and 5100 Å. The IR continuum was set at 8100, 8800, and/or 9400 Å, depending on the wavelength range covered by each NIR spectrum.

A possible origin of the disagreement between the optical and NIR continuum is a contribution from two additional NIR components (Landt et al. 2011). The first component is a diffuse continuum (due to thermal emission and scattering) that may flatten the NIR spectrum (Korista & Goad 2001). The second component is due to the finite albedo of the same dusty clouds emitting the thermal far-IR continuum (Landt et al. 2011). The small range covered by our spectra makes it impossible to measure their contributions. The continuum can be also affected by the host galaxy (this seems to be case for only one quasar in our sample, see Section 5.8).

5.2. Fe II Template

Over the years, there have been several efforts to model the ultraviolet and optical Fe II contribution (Sigut & Pradhan 2003; Sigut et al. 2004; Bruhweiler & Verner 2008). In the NIR, a semi-empirical Fe II template based on the I Zw 1 spectrum was produced by Garcia-Rissmann et al. (2012) who kindly made it available to us. A theoretical template based on photoionization was also computed by the same authors (table 3 of Garcia-Rissmann et al. 2012). A comparison of the two templates is shown in the upper left panel of Figure 4. The agreement between the two templates is fair; both indicate significant Fe II emission around 8400, 9200 Å, and 1 μm. These features are expected to be produced through Lyα pumping of high energy levels (≈11 eV) in the Fe^+ ion, although Lyα pumping may not be the only production mechanism, and additional mechanisms are still being debated (Sigut & Pradhan 1998; Rudy et al. 2000; Rodríguez-Ardila et al. 2002a; Garcia-Rissmann et al. 2012). Lyα fluorescence makes the difference between optical and NIR emission. Currently, we do not have evidence that this process could induce a difference between the NIR Fe II spectrum of Pop. A and B sources. We considered Fe II measures of table 6 of Landt et al. (2008) for Pop. A (13) and B (4) sources. The median Fe II relative intensities measured in the range 8000–9810 Å are almost identical.

The upper right side of Figure 4 shows an example of fits to the same spectrum (HE1349+0007) using different templates. The lower panels of Figure 4 show the HE1349+0007 NIR spectral range after background subtraction to illustrate the effect of the Fe II template on O I λ8446 and CaT measures.

In our spectra with high S/N, we observe a rather symmetrical bump due to Pa9 + Fe II at ≈9200 Å. The emission on the blue side of this bump cannot be reproduced with the semi-empirical template. The width of Pa9 is limited by the assumption that it should be consistent with that measured for the Balmer lines in the optical spectra. For this reason, we could not model Pa9 with a profile broad enough to fill the observed excess emission. In addition, higher-order Paschen lines constrain the Pa9 intensity. Therefore, the excess of emission with respect to the semi-empirical template has to be ascribed to Fe II. Given the problem with the semi-empirical template, the Fe II emission of our spectra was fitted with both the semi-empirical and the theoretical template.

Between 8600 and 8800 Å, the semi-empirical template presents a contribution that is not modeled by the theoretical

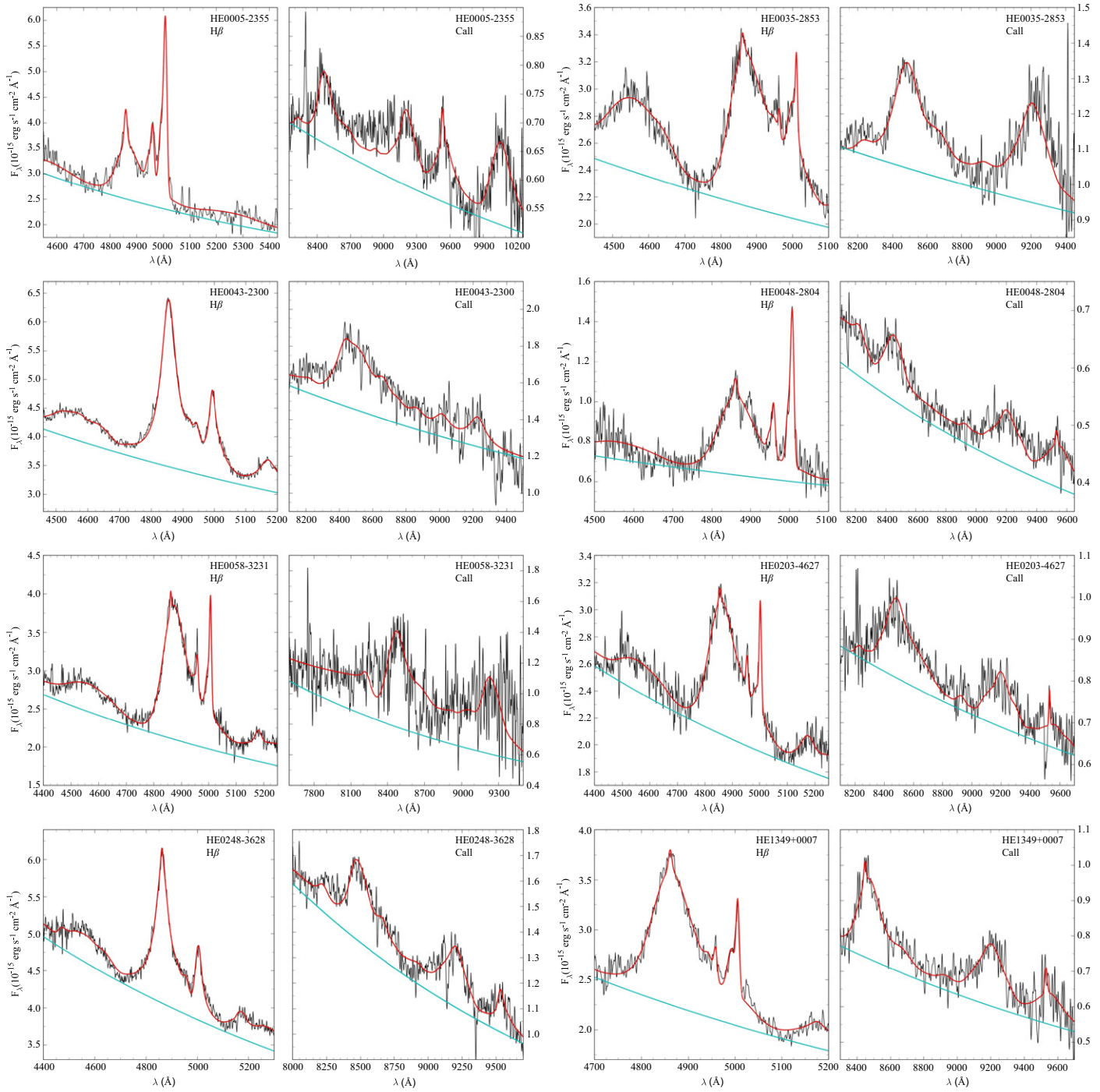

Figure 2. Calibrated spectra. Pairs of close panels show the Hβ (left) and Ca II (right) spectral regions before continuum subtraction for each object of our sample. In both panels, the best fit is marked by the red color line and the continuum level is marked with the cyan line. Abscissae are rest-frame wavelength in Å and ordinates are rest-frame specific flux in units of 10^{-15} erg s^{-1} cm^{-2} Å^{-1}.

one. This feature affects the flux and equivalent width of the line Ca II λ 8662 Å. Because the three lines have the same intensity, if the semi-empirical template is used, the equivalent width and flux of CaT and O I λ8446 decrease. In our sample, the O I λ8446 and CaT flux and equivalent widths are affected by less than 20%, save for two sources where the difference reaches ≈20–35% for O I λ8446 (HE2340–4443 and HE0203–4627), and four sources where CaT differs by 20–35% (HE0203–4627, HE2352–4010, HE0248–3628, and HE2340–4443).

We then choose the template that gave the minimum χ^2_ν value. We found that the theoretical template is better suited for the majority of the cases. In only three cases (HE2147–3212, HE2349–3800, and HE2352–4010) was the semi-empirical template used; in the remaining sources, the theoretical template was applied.

In the IR, the strongest, most isolated Fe II emission features are around 1 μm, but this wavelength range is not covered by our spectra. In the wavelength range covered by our spectra, we have no truly isolated Fe II features. However, we could still

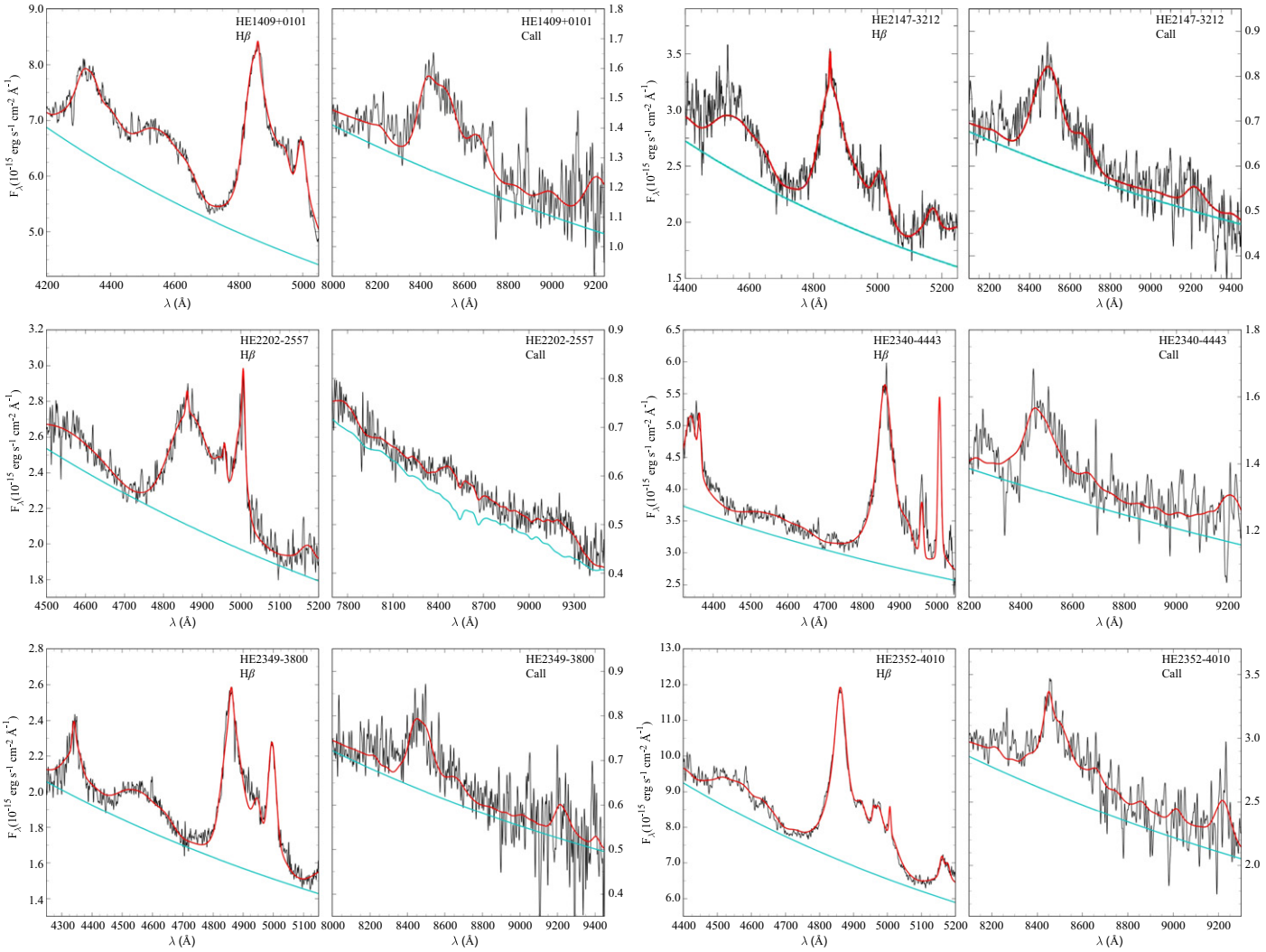

Figure 2. (Continued.)

accurately measure the Fe II contribution in the range of 9000–9400 Å from the scaled and broadened template, and consider it as an estimate of the NIR Fe II emission. In the majority of our spectra, we were able to neatly fit the Fe II and Paschen 9 line contribution.

For the Fe II optical contribution in the Hβ region we used the template previously employed by Marziani et al. (2009), mainly based on a high S/N optical spectrum of I Zw 1. Iron emission gives rise to a fairly isolated bump at ∼4450–4680 Å. Optical Fe II emission was defined by the total emission in this range (conventionally indicated with Fe II λ4570), which is a standard practice (Boroson & Green 1992).

5.3. Broad Component

Following the 4DE1 approach (Sulentic et al. 2000a, 2000b, 2007; Marziani et al. 2001, 2003a, 2003b), we assume that low-ionization lines in Pop. A and B sources have profiles that are best fitted by Lorentzian (Pop. A) or double Gaussian (Pop. B). All the BCs were modeled with this assumption. We note that the Lorentzian approach is roughly equivalent to fitting two Gaussians with the same shifts (usually $\lesssim$200 km s^{-1} for Pop. A sources, Sulentic et al. 2012), one broader and one narrower. However, this is strictly true if the S/N is low: at very high S/N (not the case of our data), a Lorentz function yields a lower χ_ν^2 (Marziani et al. 2003b). Since the best data suggest that Pop. A Hβ profiles are Lorentzian (Véron-Cetty et al. 2001; Marziani et al. 2003b; Zamfir et al. 2010; Shapovalova et al. 2012), we fit Lorentzian functions to the broad line profiles of all Pop. A sources in our sample. With a double Gaussian fit, the difference between Pop. A and B would be that the broader Gaussian is usually redshifted in Pop. B.

The Hβ line profile was taken as a reference for modeling the CaT and O I λ8446 blend, since its profile is well defined and well understood. CaT was modeled with three BCs of equal intensity and the same FWHM since it is believed that the Ca II triplet components are optically thick (Persson 1988; Ferland & Persson 1989). As Ca II lines are completely blended, it is difficult to measure a shift, so that the Ca II lines were held fixed at rest-frame wavelength. The maximum shifts possible for O I λ8446 were the ones measured on Hβ due to the relation between the two lines (see also Section 7.1). FWHM and shifts of Hβ and high-order Paschen lines were assumed to be identical within the uncertainties.

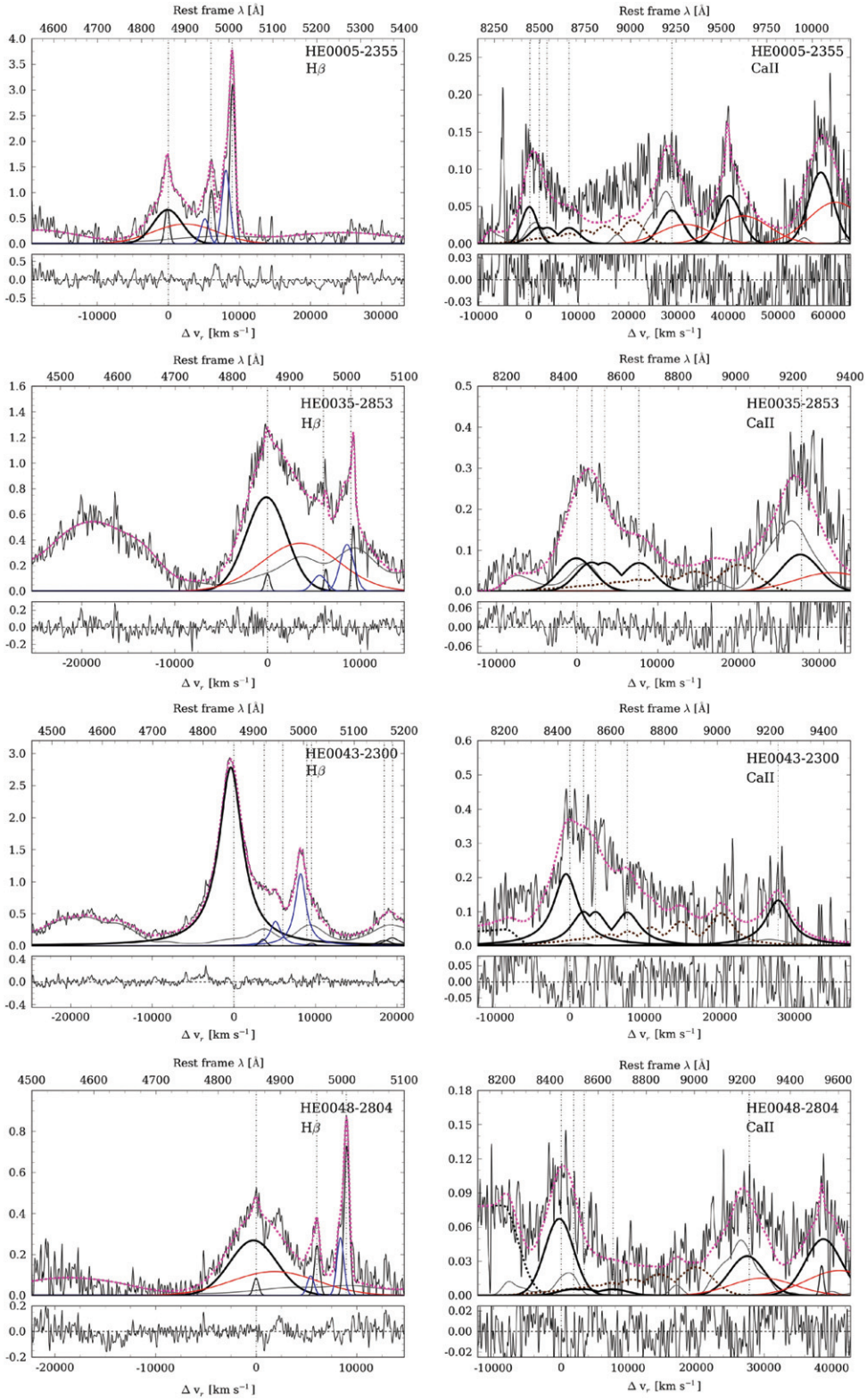

Figure 3. Quasar spectra after continuum subtraction. Abscissae are rest-frame wavelength in Å and ordinates are rest-frame specific flux in units of 10^{-15} erg s^{-1} cm^{-2} Å^{-1}. The left panels show the Hβ spectral region and the right panels show the Ca II triplet spectral region. The vertical dashed lines are the rest frame Hβ, [O III] $\lambda\lambda$4959, 5007, O I λ8446 and Ca II λ8498, λ8542, λ8662. Line coding is as follows. Thick black lines: broad components; thin black lines: narrow components; blue lines: blueshifted components of Hβ; red lines: Hβ and Pa9 VBC; gray lines: Fe II contribution; thick dashed black lines: Paschen continuum; thick-brown lines: high-order Paschen lines; thin-dashed pink lines: best-fit model. Note that the Ca II triplet and high-order Paschen lines are shown as blends of individual lines and not as their sum.

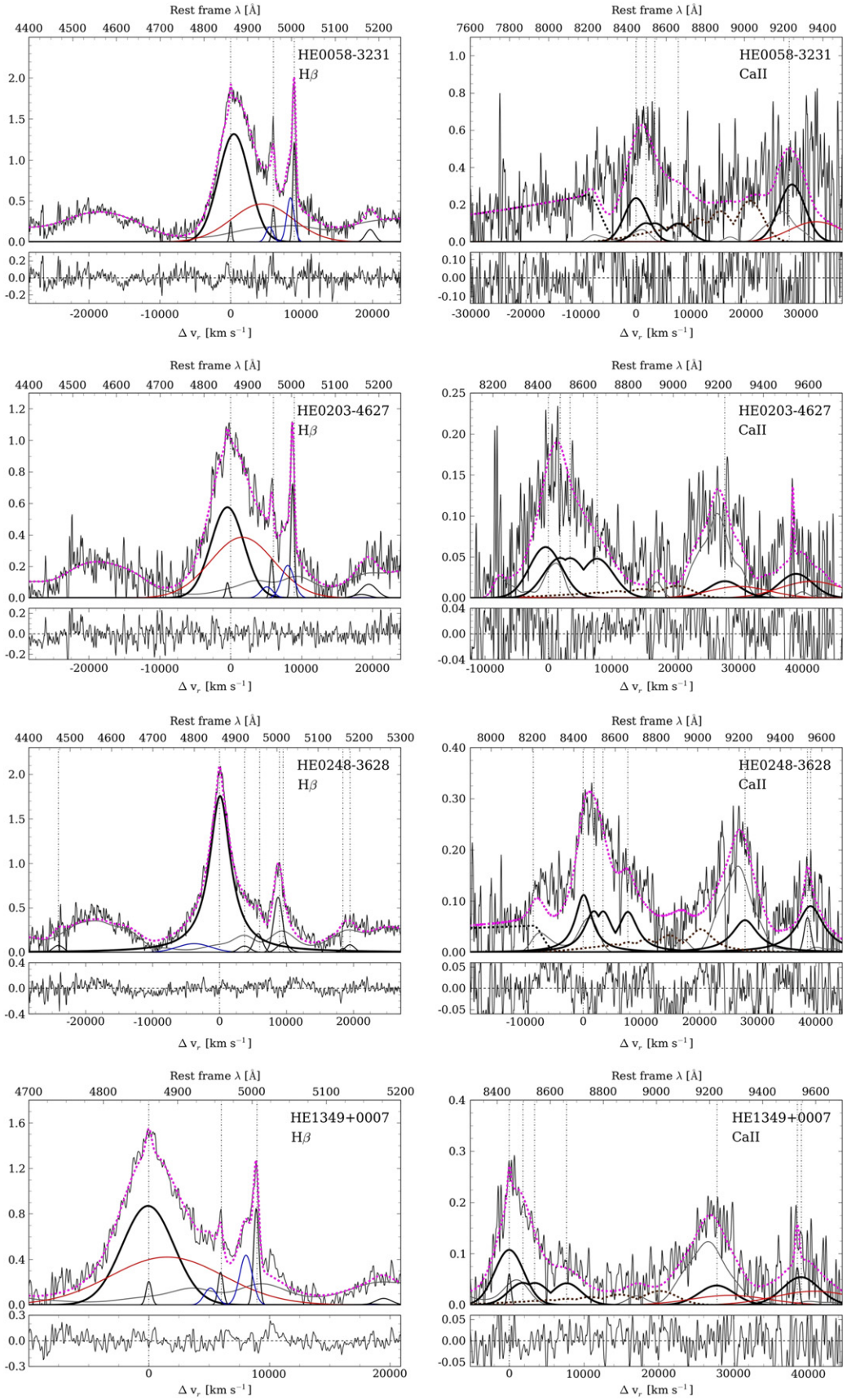

Figure 3. (Continued.)

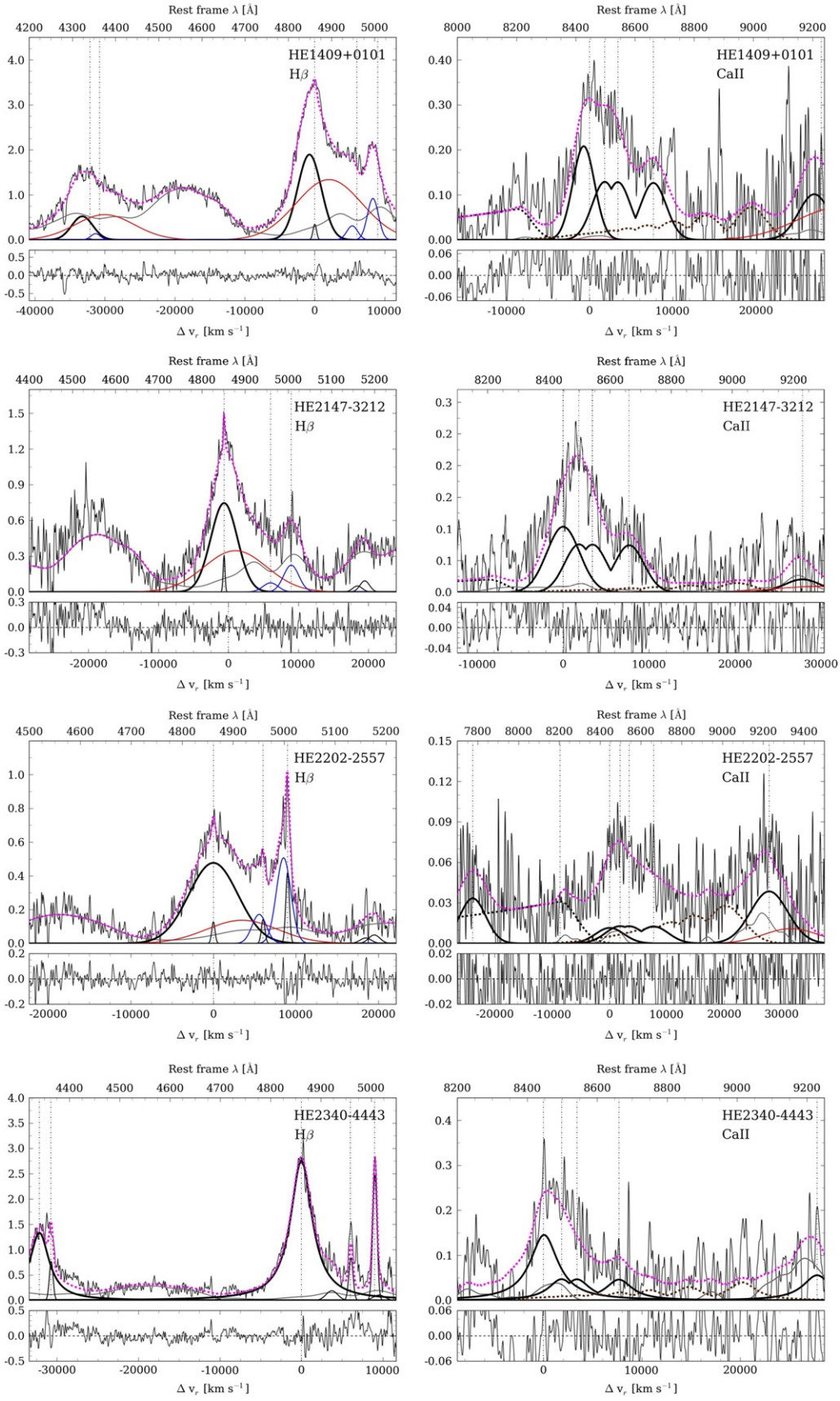

Figure 3. (Continued.)

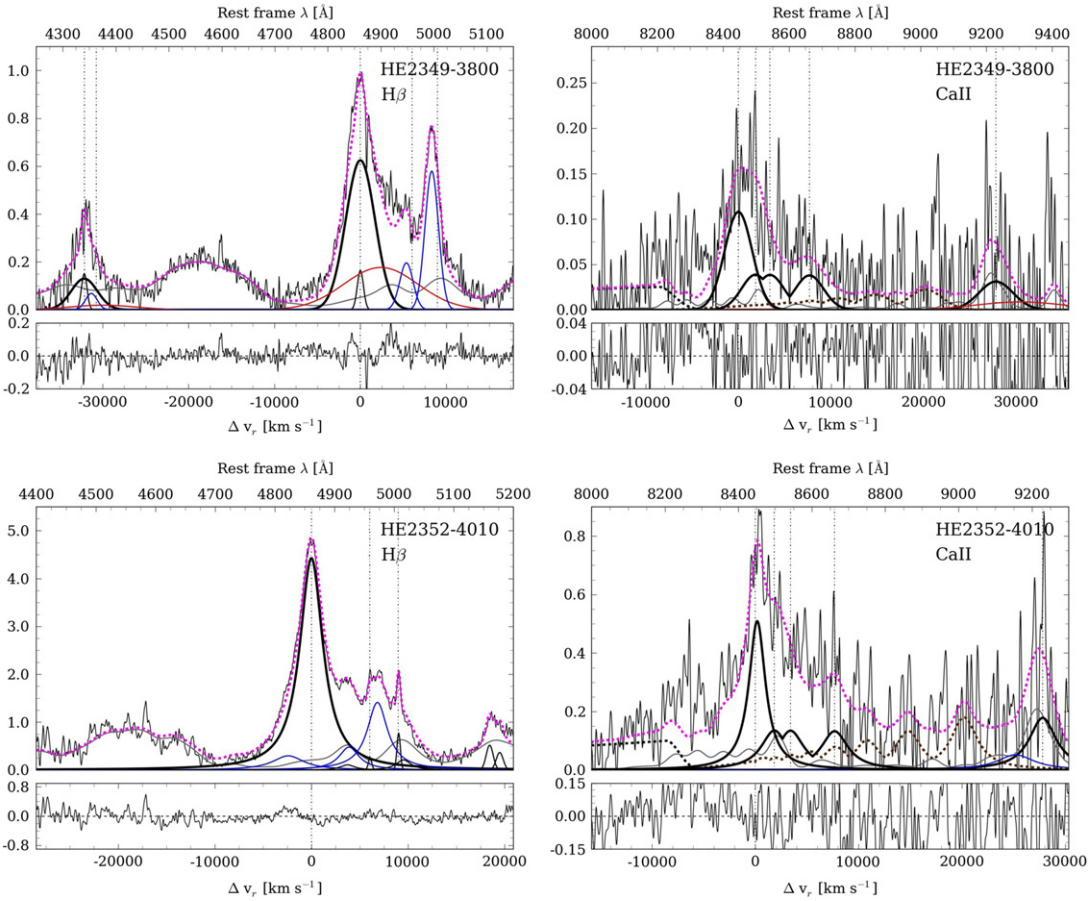

Figure 3. (Continued.)

5.4. Very Broad Component

A VBC was fitted to Hβ and the most intense high-order Paschen lines (Pa9, Paϵ λ9546, and Paδ λ10049) for all Pop. B sources. The shift and FWHM were assumed equal to those of Hβ within the uncertainties. A VBC was not fit to the Ca II triplet, since the VBC is believed to be associated with a very high ionization region (the very broad line region, VBLR, e.g., Snedden & Gaskell 2007 and Marziani et al. 2010) that is expected to emit negligible Fe II and Ca II. Since there is no clear spectroscopic evidence of the presence of a VBC for O I, only a BC was first considered also for this line (although the possibility of an O I VBC is debatable and discussed in section Section 7.2).

5.5. Narrow Components (NCs) and Narrow Lines

We considered the Hβ NC (H$\beta_{\rm NC}$) and [O III] $\lambda\lambda$4959, 5007. In the NIR, we were able to detect a hint of the NC for O I only in HE1349+0007, a source in which H$\beta_{\rm NC}$ is especially strong. Also, in all the spectra covering the region around ∼9500 Å, we could detect [S III] λ9531.

5.6. High-order Paschen Lines

Modeling the NIR spectral range with only the strongest high-order Paschen lines visible in our spectra (Pa9 λ9229, Paϵ λ9546, and Paδ λ10049) results in an emission deficit between 8700 and 9100 Å. Therefore we decided to include even higher-order Paschen lines: from Pa9 λ9229 up to Pa24 λ8334. Since Pa9 is clearly seen in the majority of our spectra, it was taken as a reference to scale the intensity of the other Paschen lines. The intensity ratios were computed from case B values from CLOUDY simulations (version 08.00; Ferland et al. 1998, 2013) which have an exponential decay with increasing order number. This set of lines forms a pseudo-continuum that cannot be neglected in some cases. Previously, Persson (1988) found that Paschen lines contribute ∼12% of the flux of Ca II λ8662 in Mrk 42, so that they were ignored. Comparing the flux of Pa13 λ8665 and the Ca II λ8662, we found that Paschen lines do contribute by a fraction $\gtrsim$ 30% in 10 sources; in 2 sources, the contribution is ∼10% (HE0203–4627 and HE2147–3212). In two cases (HE0048–2804 and HE0058–3231), the high-order Paschen lines dominate the fit.

5.7. Paschen Continuum

We could detect a hint of PaC in HE0048–2804 and HE2202–2557, so we included an optically thin model of PaC at 8204 Å. The inclusion has little effect on the O I λ8446 and CaT measures, since the Paschen series head is separated in wavelength from the O I + CaT blend. A CLOUDY simulation with $\log U = -2.5$ and $\log n_{\rm H} = 12$ provided us with predictions on the relative intensity of Pa9 and of the integrated PaC (see Osterbrock & Ferland 2006). We then estimated the continuum specific intensity at the Paschen edge and assumed an exponential decrease toward shorter wavelengths appropriate for an optically thin case. Our estimates appear to be in

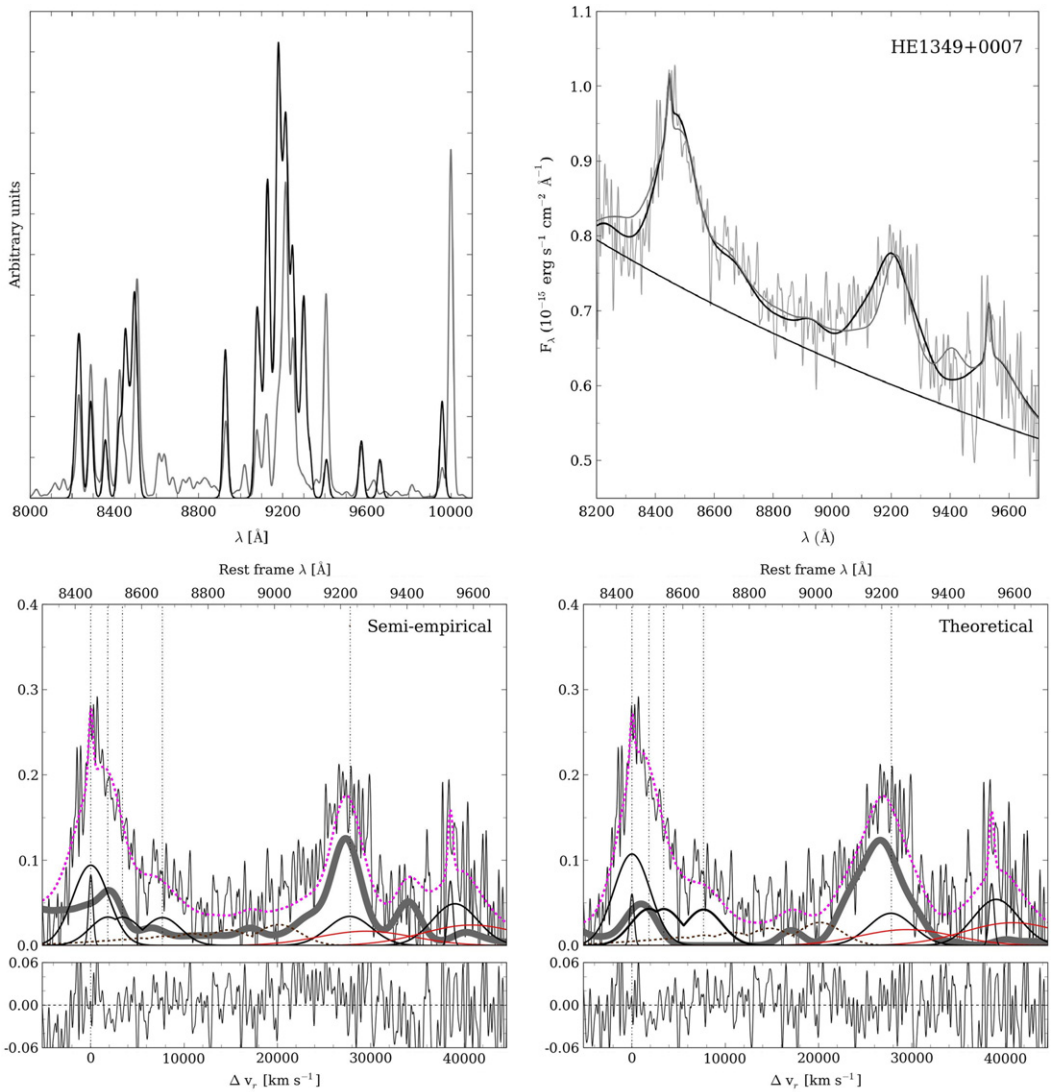

Figure 4. Upper left panel: comparison between theoretical (black line) and semi-empirical (gray line) templates, as obtained by Garcia-Rissmann et al. (2012). Upper right panel: models of the NIR spectral region for HE1349+0007 using the two templates. The Fe II prominent feature at ∼9200 Å is less strong in the semi-empirical template, leaving a flux deficit in the observed blend with Pa9 λ9229. The lower panels emphasize the difference between the two Fe II templates (thick gray line; left: semi-empirical, right: theoretical). Line coding is the same as for the previous figure.

excess with respect to the observations since the best fits require a PaC smaller than that predicted. There are three main possible explanations: (1) CLOUDY computations over-predict the recombination continuum (a distinctly possible case since the assumed conditions are unlikely to be found in optically thin gas), (2) the quasar continuum level is not correct, and the actual continuum is lower, or (3) PaC is not optically thin. We cannot test these options on our data since the spectra cover only a small wavelength range. To properly define PaC, we need to cover a spectral range spanning from the optical to the NIR. We will try to address the issue of the PaC intensity in the future.

5.8. Contribution of the Host Galaxy

A new stellar population synthesis model (Y. Chen et al. 2015, in preparation), based on the code of Bressan et al. (1998) with updated stellar evolutionary tracks (Bressan et al. 2012) and with stellar atmospheres was used to account for the possible contribution of the quasar host galaxy. These computations are suitable for the analysis of stellar absorption lines in the optical and NIR spectral regions (Sánchez-Blázquez et al. 2006a, 2006b, 2006c; Rayner et al. 2009). From the lookback time at the quasar redshift, we estimated an upper limit to the host age. Then we computed the black hole mass, and estimated the host mass assuming the $M_{\rm bulge}/M_{\rm BH}$ ratio (Magorrian et al. 1998; Merloni et al. 2010) appropriate for the quasar redshift. The 0.9 μm specific flux was then derived from the stellar population synthesis models that are provided as a function of mass. We found that the underlying stellar absorption of the host galaxy is significant only in HE2202–2557 with a luminosity contribution of ≈50%, while the rest of the sample is affected only by $\lesssim$10%. In the HE2202–2557 case, we assumed a spheroid mass ≈1.1 $\times$ $10^{12} M_{\odot}$, an age of 2.4 Gyr, and a metallicity of $2Z_{\odot}$. These properties are consistent with massive ellipticals expected to host very luminous quasars at intermediate redshift (Trager et al. 2000; Kukula et al. 2001; Sánchez et al. 2004; Falomo

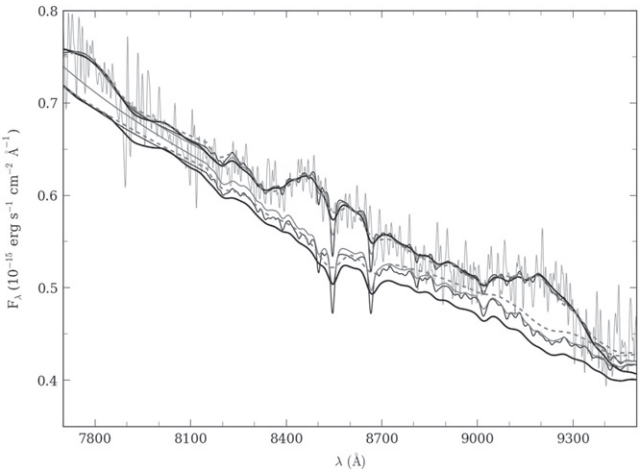

Figure 5. Stellar contribution of HE2202–2557 using different spheroid masses. The thin black and gray lines mark host galaxies with masses of 10^{10} and 10^{11} $M_\odot$, respectively. The thick black line marks the host galaxy with a mass of 10^{12} $M_\odot$. The dashed gray line indicates the galaxy with the higher mass 10^{13} $M_\odot$. Metallicity $2Z_\odot$ and age 2.4 Gyr are assumed in all cases. Abscissae are rest-frame wavelength in Å, ordinates are rest-frame specific flux in units of 10^{-15} erg s^{-1} cm^{-2} Å^{-1}.

et al. 2004; Kotilainen et al. 2007; Spolaor et al. 2009; Floyd et al. 2013).

In order to test the behavior of several stellar templates, we performed several models taking different spheroid masses (10^{10}, 10^{11}, 10^{12}, 10^{13} $M_\odot$, but keeping metallicity equal to $2Z_\odot$, and host age 2.4 Gyr). Model spectra with different spheroid masses provide a similar total spectrum, but spectra differ in the CaT range where the stellar absorptions have different depths and widths, as shown in Figure 5. The CaT intensity in absorption decreases with increasing galaxy mass and/or velocity dispersion (Cenarro et al. 2003; van Dokkum & Conroy 2012) while its width increases. These changes affect the emission lines measurements. The flux and equivalent width of CaT in emission and of O I λ8446 increase with galaxy mass. The effect induced by a three orders of magnitude mass change is, in general, $\lesssim$50%. In the HE2202–2557 case, Figure 5 shows that host masses lower than 1×10^{12} $M_\odot$ would yield significant residuals and a worse χ_ν^2, while for $1 \times 10^{13} M_\odot$ the χ_ν^2 will not change significantly. We assume a bulge mass 1.1×10^{12} $M_\odot$, consistent with the value expected from $M_{\rm bulge}/M_{\rm BH}$ ratio at intermediate redshift following Merloni et al. (2010).

6. RESULTS

Figure 3 shows the multicomponent fits after continuum subtraction for the Hβ and O I λ8446 + CaT spectral regions. Results of multicomponent fits are provided in Tables 2 and 3. Table 2 reports Hβ and Pa9 λ9229 measurements. The first column lists the name of the object and the second column is the continuum flux measured at the line's rest-frame. The next columns list equivalent width (W), flux (F), and FWHM for BC, NC, and VBC. The last column reports the FWHM of the full profile, i.e., the sum of BC and VBC. Table 3 reports the O I λ8446 and CaT λ8498, λ8542, and λ8662 measurements. As for Table 2, the second column lists the continuum flux at the O I λ8446 wavelength and the other columns report W, flux, and FWHM for the BCs. The NC was detected for O I only in the case of HE1349+0007. Error estimates were obtained as described in Appendix B. The equivalent width and flux for optical and NIR Fe II are reported in Table 4. The last column reports which NIR template (i.e., theoretical or semi-empirical) was used in the fits. Shifts are, at first guess, assumed to be consistent with those of Hβ, and are found to be in general close to zero (i.e., consistent with the quasar rest frame). They are therefore not reported. Only in one case, HE1409+0101, does $H\beta_{\rm BC}$ show a significant blueshift, −700 km s^{-1}, and a similar shift was applied to the O I peak to make it consistent with Hβ. The Ca II triplet was assumed to always be at rest frame. The VBC of hydrogen lines was fit with a broad Gaussian that has a large shift to the red, ∼1000–3000 km s^{-1}, assumed to be the same for the optical and NIR hydrogen lines.

6.1. Ca II Triplet Detection

The Ca II triplet has been observed in sources with strong Fe II emission, as in the majority of the Persson (1988) sample. CaT could be observed in many Fe II strong sources because they are narrow line Seyfert 1s, and emission lines are therefore relatively narrow (FWHM Hβ $\lesssim$ 2000 km s^{-1}) and sharply peaked. In our sources, CaT lines are often broad and totally blended with O I λ8446 and high-order Paschen lines, making it necessary to confirm that CaT is really detected. The λ8498 and λ8542 lines do not provide conclusive evidence because they are heavily blended among themselves and with O I λ8446. On the other hand, Ca II λ8662 is in a region relatively free from strong contaminating lines, and in some cases this line could be detected by a simple visual inspection of the spectra (HE0248–3628 is an example). In two cases of sources with weak CaT, like HE0048–2804 and HE2202–2557, visual inspection is inconclusive. To test whether or not detections are real, we performed a fit with no CaT emission. In HE0048–2804, we could observe a slightly positive residual around 8600 Å; CaT emission is very weak, if there is any at all (Figure 6, left). The positive residual is strong in HE2202–2557 and without any doubt that CaT emission is present (Figure 6, right). We conclude that the Ca II triplet is detected in all of our sources with the possible exception of HE0048–2804, even if the detection of CaT emission was not a priori expected on the basis of the Fe II–Ca II correlation (Persson 1988; Joly 1989; Ferland & Persson 1989; Dultzin-Hacyan et al. 1999). We also note that W(CaT) can be as large as ≈50 Å.

6.2. Relations between Ca II Triplet and O I λ8446

The equivalent width distributions of CaT and O I λ8446 for Persson (1988) and our sample are shown in the upper panels of Figure 7. The spread of O I λ8446 and CaT values is similar in the two samples. In our sample, W(CaT) is distributed over a wide range, whereas the W(O I) distribution is peaked around ≈15–20 Å. The Persson sample similarly shows a narrower distribution of W(O I λ8446). The difference in the equivalent width distributions is reflected in the wide range of the CaT/O I λ8446 ratio: from almost 0 to CaT significantly stronger than O I λ8446.

If we add the 11 upper limits in the sample of Persson (1988) to the distribution, then the CaT seems to be significantly more prominent in our sample. Two sample tests that include censored data indicate a confidence level between 0.92 (Gehan's Generalized Wilcoxon test) and 0.98 (Logrank

Table 2
Measurements of Equivalent Width, Flux, and FWHM of Hβ and Pa9 Lines

Object Name	f_λ (erg s^{-1} cm^{-2} Å^{-1})	BC			NC			VBC			Full Profile
		W(Å)	F (erg s^{-1} cm^{-2})	FWHM (km s^{-1})	W(Å)	F (erg s^{-1} cm^{-2})	FWHM (km s^{-1})	W(Å)	F (erg s^{-1} cm^{-2})	FWHM (km s^{-1})	FWHM (km s^{-1})
					Hβ						
HE0005–2355	2.5 ± 0.1	21.8 ± 2	54.6 ± 5	4780 ± 710	3.7 ± 0.4	9.3 ± 1.0	790 ± 120	28.7 ± 9	70.5 ± 21	10490 ± 1550	5810 ± 340
HE0035–2853	2.1 ± 0.1	30.3 ± 1	65.0 ± 2	5140 ± 390	0.7 ± 0.1	1.5 ± 0.1	620 ± 50	30.2 ± 5	63.4 ± 9	9690 ± 740	6200 ± 190
HE0043–2300	3.5 ± 0.2	69.3 ± 5	247.7 ± 12	3500 ± 110	...	...	...	–	–	–	3500 ± 110
HE0048–2804	0.6 ± 0.03	40.1 ± 4	25.4 ± 2	5500 ± 470	1.4 ± 0.2	0.9 ± 0.1	620 ± 90	32.4 ± 6	20.3 ± 4	10000 ± 1480	6610 ± 380
HE0058–3231	2.1 ± 0.1	55.4 ± 2	116.7 ± 3	5130 ± 160	0.8 ± 0.1	1.7 ± 0.1	390 ± 30	39.9 ± 7	81.3 ± 13	10010 ± 390	6200 ± 190
HE0203–4627	2.1 ± 0.1	26.1 ± 3	54.4 ± 5	5490 ± 810	0.4 ± 0.1	0.9 ± 0.1	550 ± 80	34.1 ± 10	70.0 ± 21	10490 ± 900	6630 ± 380
HE0248–3628	4.1 ± 0.1	40.7 ± 2	170.0 ± 7	3800 ± 150	0.6 ± 0.1	2.3 ± 0.4	600 ± 50	2.4 ± 1*	10.0 ± 3*	6000 ± 460*	4460 ± 170*
HE1349+0007	2.3 ± 0.1	33.5 ± 4	75.5 ± 7	5030 ± 430	0.8 ± 0.1	1.9 ± 0.2	530 ± 80	36.2 ± 11	80.1 ± 24	10980 ± 430	6110 ± 350
HE1409+0101	4.9 ± 0.1	26.8 ± 1	130.5 ± 2	4000 ± 160	0.7 ± 0.03	3.6 ± 0.1	600 ± 20	53.8 ± 2	256.0 ± 11	11000 ± 110	4840 ± 50
HE2147–3212	2.0 ± 0.1	28.4 ± 3	57.7 ± 6	4490 ± 660	0.8 ± 0.1	1.7 ± 0.2	310 ± 50	31.6 ± 10	63.1 ± 19	10520 ± 1560	5470 ± 320
HE2202–2557	2.1 ± 0.1	27.4 ± 1	57.6 ± 2	7000 ± 540	0.5 ± 0.04	1.0 ± 0.1	470 ± 40	11.7 ± 2	23.9 ± 4	9990 ± 760	8030 ± 310
HE2340–4443	2.8 ± 0.1	77.5 ± 3	224.6 ± 6	3200 ± 100	...	...	...	–	–	–	3200 ± 100
HE2349–3800	1.6 ± 0.03	27.1 ± 1	43.1 ± 1	4000 ± 160	1.5 ± 0.1	2.4 ± 0.1	850 ± 30	19.8 ± 3	31.0 ± 4	10060 ± 410	4870 ± 150
HE2352–4010	7.1 ± 0.1	45.3 ± 1	327.0 ± 9	2900 ± 90	...	...	...	4.0 ± 0.1*	30.0 ± 2*	4000 ± 162*	3300 ± 30*
					Pa9 λ9229						
HE0005–2355	0.6 ± 0.02	11.9 ± 5 (5)	7.0 ± 3 (3)	4770 ± 2690 (3500)	...	...	...	15.6 ± 3 (5)	9.1 ± 2 (3)	10500 ± 2410 (3210)	5800 ± 3270 (4360)
HE0035–2853	0.9 ± 0.01	15.8 ± 2 (2)	18.0 ± 2 (2)	5120 ± 1020 (1450)	...	...	...	12.7 ± 1 (1)	14.6 ± 1 (1)	9700 ± 740 (800)	6170 ± 3070 (3570)
HE0043–2300	1.3 ± 0.03	18.0 ± 6 (6)	23.5 ± 8 (8)	3660 ± 1640 (1810)	...	...	...	–	–	–	3660 ± 1640 (1810)

Table 2
(Continued)

Object Name	f_λ (erg s^{-1} cm^{-2} Å^{-1})	BC			NC			VBC			Full Profile
		W(Å)	F (erg s^{-1} cm^{-2})	FWHM (km s^{-1})	W(Å)	F (erg s^{-1} cm^{-2})	FWHM (km s^{-1})	W(Å)	F (erg s^{-1} cm^{-2})	FWHM (km s^{-1})	FWHM (km s^{-1})
HE0048–2804	0.4 ± 0.01	14.6 ± 2 (2)	6.3 ± 1 (1)	5550 ± 1250 (2400)	...	...	...	11.9 ± 1 (9)	5.0 ± 0.2 (0.3)	9980 ± 880 (1690)	6650 ± 1000 (1920)
HE0058–3231	0.6 ± 0.06	86.3 ± 13 (13)	51.9 ± 5 (5)	5130 ± 770 (1520)	...	...	...	62.0 ± 9 (9)	36.3 ± 3 (4)	10020 ± 1590 (3140)	6200 ± 930 (1840)
HE0203–4627	0.7 ± 0.03	5.3 ± 4 (4)	3.7 ± 3 (3)	5500 ± 3180 (3670)	...	...	...	6.9 ± 4 (4)	4.7 ± 2 (3)	10200 ± 2340 (2700)	6610 ± 3730 (4300)
HE0248–3628	1.1 ± 0.02	12.8 ± 0.4 (0.4)	14.9 ± 0.3 (0.3)	4900 ± 500 (500)	...	...	...	–	–	–	4900 ± 500 (500)
HE1349+0007	0.6 ± 0.02	10.6 ± 6 (7)	6.3 ± 4 (4)	5100 ± 3010 (2850)	...	...	...	11.4 ± 3 (5)	6.7 ± 2 (3)	10860 ± 720 (730)	6190 ± 3300 (3320)
HE1409+0101	1.1 ± 0.04	12.6 ± 5 (5)	13.4 ± 5 (5)	4030 ± 2270 (2200)	...	...	...	15.6 ± 5 (6)	26.2 ± 5 (6)	10990 ± 2400 (2440)	4870 ± 710 (730)
HE2147–3212	0.5 ± 0.02	6.0 ± 4 (4)	3.0 ± 2 (2)	4500 ± 2600 (3450)	...	...	...	6.3 ± 4 (4)	3.3 ± 1 (1)	10520 ± 2410 (3190)	5470 ± 3170 (4190)
HE2202–2557	0.2 ± 0.004	20.1 ± 4 (5)	8.8 ± 1 (1)	6990 ± 1050 (1040)	...	...	...	8.5 ± 2 (2)	3.3 ± 0.3 (0.3)	10000 ± 1290 (1290)	8020 ± 3020 (3070)
HE2340–4443	1.2 ± 0.05	5.5 ± 5 (5)	8.6 ± 6 (6)	3200 ± 1430 (1450)	...	...	...	–	–	–	3200 ± 1430 (1450)
HE2349–3800	0.4 ± 0.02	7.7 ± 6 (6)	4.0 ± 3 (3)	3940 ± 2280 (2380)	...	...	...	5.2 ± 3 (4)	2.9 ± 2 (2)	10060 ± 2310 (2400)	4780 ± 2770 (2880)
HE2352–4010	2.1 ± 0.04	11.2 ± 3 (3)	25.0 ± 6 (6)	2900 ± 1110 (1070)	...	...	...	4.3 ± 0.4 (0.4)*	10.0 ± 1 (1)	4020 ± 450 (430)	3300 ± 470 (490)

Notes. [1]The asterisk (*) indicates Pop. A sources with a BC blueshifted component. [2]The component that was not observed is marked by ellipsis (···). [3]The dashed line (–) indicates that the component is not appropriated for this kind of source. [4]In parentheses, we report the uncertainty taking into account the Fe II template effect. See Appendix B. In some cases, the uncertainty appears below the value.

Table 3
Measurements of Equivalent Width, Fluxes, and FWHM of O I λ8446 and Ca II Triplet

Object Name	f_λ (erg s^{-1} cm^{-2} Å^{-1})	BC		
		W (Å)	F (erg s^{-1} cm^{-2})	FWHM (km s^{-1})
		O I λ8446		
HE0005–2355	0.7 ± 0.03	7.8 ± 2 (2)	5.2 ± 1 (1)	3500 ± 820 (1080)
HE0035–2853	1.0 ± 0.02	9.4 ± 2 (2)	12.1 ± 2 (2)	5000 ± 370 (410)
HE0043–2300	1.5 ± 0.03	24.5 ± 3 (3)	37.1 ± 4 (5)	4000 ± 360 (390)
HE0048–2804	0.5 ± 0.01	18.4 ± 1 (2)	10.1 ± 1 (1)	4990 ± 270 (500)
HE0058–3231	0.8 ± 0.08	44.4 ± 8 (8)	35.0 ± 5 (5)	4960 ± 100 (100)
HE0203–4627	0.8 ± 0.03	13.6 ± 3 (4)	11.1 ± 3 (3)	6000 ± 250 (250)
HE0248–3628	1.4 ± 0.02	12.2 ± 2 (2)	17.3 ± 3 (3)	3490 ± 260 (260)
HE1349+0007	0.7 ± 0.03	19.9 ± 4 (5)	14.7 ± 3 (4)	4580 ± 680 (850)*
HE1409+0101	1.3 ± 0.05	15.3 ± 2 (2)	19.3 ± 3 (3)	3100 ± 310 (310)
HE2147–3212	0.6 ± 0.02	22.1 ± 6 (11)	13.6 ± 4 (7)	4300 ± 860 (1450)
HE2202–2557	0.3 ± 0.01	3.6 ± 1 (3)	2.0 ± 0.4 (1)	5810 ± 1060 (1370)
HE2340–4443	1.3 ± 0.05	15.9 ± 1 (2)	22.0 ± 2 (2)	3430 ± 220 (220)
HE2349–3800	0.6 ± 0.02	17.6 ± 4 (5)	11.3 ± 2 (3)	3480 ± 520 (520)
HE2352–4010	2.6 ± 0.05	16.6 ± 2 (3)	43.5 ± 4 (4)	1930 ± 110 (110)
		Ca II λ8498, λ8542, λ8662		
HE0005–2355	0.7 ± 0.03	13.9 ± 8 (11)	9.1 ± 5 (7)	4600 ± 1070 (1690)
HE0035–2853	1.0 ± 0.02	27.9 ± 2 (2)	28.8 ± 2 (2)	4540 ± 170 (180)
HE0043–2300	1.4 ± 0.03	36.1 ± 3 (4)	53.3 ± 4 (6)	4000 ± 150 (160)
HE0048–2804	0.5 ± 0.01	4.9 ± 3 (4)	2.6 ± 2 (2)	5170 ± 2400 (3200)
HE0058–3231	0.8 ± 0.08	59.6 ± 14 (21)	45.0 ± 10 (15)	4910 ± 740 (750)
HE0203–4627	0.8 ± 0.03	33.2 ± 3 (4)	26.3 ± 3 (3)	5960 ± 530 (650)
HE0248–3628	1.3 ± 0.02	31.3 ± 2 (2)	42.8 ± 2 (3)	3990 ± 150 (150)
HE1349+0007	0.7 ± 0.03	24.7 ± 7 (7)	17.7 ± 5 (5)	4530 ± 940 (1100)
HE1409+0101	1.2 ± 0.05	19.9 ± 6 (7)	41.4 ± 8 (8)	3550 ± 500 (510)
HE2147–3212	0.6 ± 0.02	47.4 ± 4 (5)	28.1 ± 2 (3)	3990 ± 150 (150)
HE2202–2557	0.3 ± 0.01	13.0 ± 3 (4)	6.8 ± 1 (1)	5900 ± 330 (400)
HE2340–4443	1.3 ± 0.05	14.8 ± 10 (11)	20.1 ± 14 (15)	3190 ± 1700 (1760)
HE2349–3800	0.6 ± 0.02	19.9 ± 6 (6)	12.3 ± 3 (3)	3520 ± 700 (730)
HE2352–4010	2.5 ± 0.05	21.7 ± 3 (3)	55.7 ± 6 (6)	3080 ± 180 (180)

Notes. [1]In parentheses, we report the uncertainty taking into account the Fe II template effect. [2]The equivalent width, flux, and FWHM values for O I NC are 1.3 ± 1.0 Å, 1.0 ± 0.7 erg s^{-1} cm^{-2}, and 550 ± 250 km s^{-1}, respectively.

test). The O I λ8446 distributions (no upper limit; lower left) are instead consistent. Persson (1988) fails to detect CaT emission if CaT/O I λ8446 $\lesssim$ 0.3 with W(O I λ8446) ∼ 10–20 Å. These sources all show $R_{\rm Fe\,II} \lesssim 0.5$ and are of spectral type B1 or A1. This finding leaves open the possibility that there could be a dependence on L and/or z (Section 6.5) specially for CaT.

6.3. Line Widths of Hβ, O I λ8446, and Ca II Triplet

Our data and that of Persson are complementary because our sample is mainly made of Pop. B sources (Table 1; column 6). Twelve of the Persson (1988) sources are Pop. A, for which FWHM(Hβ) $\leqslant$ 4000 km s^{-1}, and two are Pop. B. (II Zw 136 and Mrk 376). If we compare the FWHM of Hβ (measured on the full profile, without separating VBC from BC; top panel of Figure 8), we see an overall consistency of FWHM(Hβ) with FWHM(CaT) and FWHM(O I λ8446) for Pop. A sources, while for Pop. B sources FWHM(Hβ) is significantly larger than the FWHM of the NIR lines. This is the effect of the VBC that broadens the full profile of Pop. B by 20–30% (Marziani et al. 2013a).

If we restrict our attention to the BC of Hβ, there is an obvious correlation between FWHM($H\beta_{\rm BC}$) $\gtrsim$ FWHM(CaT) ∼ FWHM(O I λ8446) (middle panel of Figure 8), which confirms and extends the trend found by Persson (1988). In the middle panel of Figure 8, Pop. A sources are located around the equality line, while Pop. B sources are located below. The Pop. B trend is significant at a 2σ confidence level according to a Wilcoxon signed rank test (Wilcoxon 1945), and may indicate that there is a systematic difference between the widths of Hβ BC only and O I λ8446 or CaT in Pop. B sources. A discrepancy could also be due to different quality of data and/or to different measurement techniques, since Pop. A sources are mainly from the Persson sample and Pop. B sources are from our sample, and the Hβ profiles need a BC/VBC decomposition. If broadening is predominantly due to virial motions, and

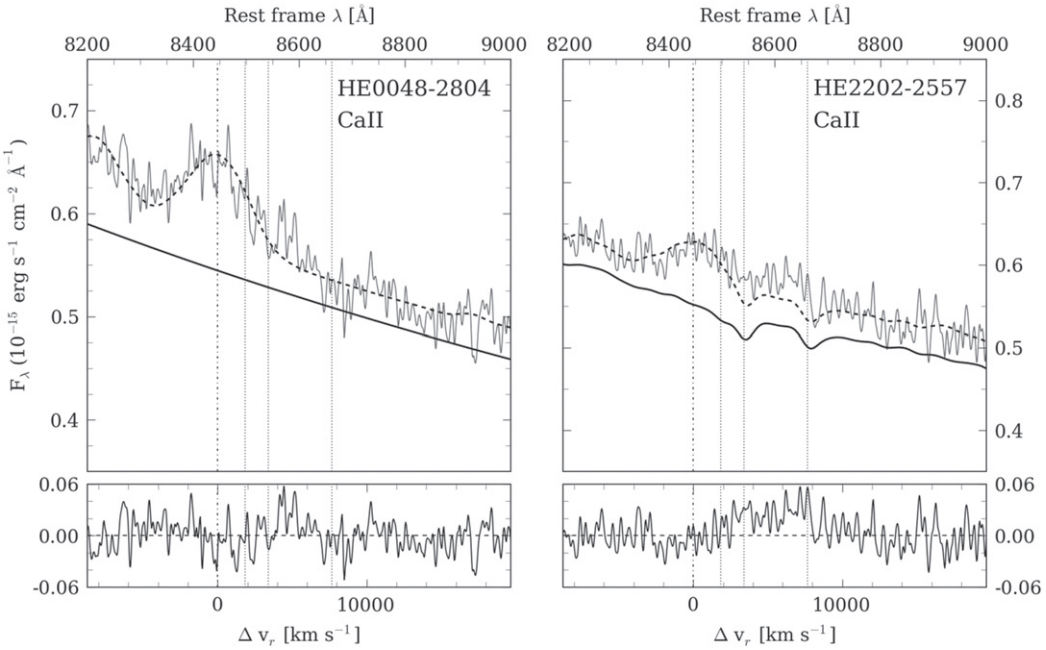

Figure 6. Quasar spectra modeled without Ca II triplet contribution but with all other features present. A positive residual at ∼8542–8662 Å indicates the presence of the Ca II triplet. Vertical dash–dot and dot lines mark O I λ8446 and Ca II λ8498, λ8542, λ8662 rest-frame wavelengths. The thick black line traces the assumed continuum (for HE2202–2557 it includes the best-fit host galaxy template).

Table 4
Measurements of Equivalent Width and Flux for Optical and NIR Fe II

Object Name	Fe II$_{opt}$		Fe II$_{NIR}$		Template Used
	W (Å)	F (erg s^{-1} cm^{-2})	W (Å)	F (erg s^{-1} cm^{-2})	
HE0005–2355	17.2 ± 2	51.4 ± 8	20.4 ± 5	12.1 ± 9	Theoretical
HE0035–2853	40.7 ± 3	97.0 ± 8	34.2 ± 4	32.5 ± 8	Theoretical
HE0043–2300	20.0 ± 1	78.7 ± 6	2.8 ± 0.3	3.5 ± 0.2	Theoretical
HE0048–2804	22.3 ± 2	15.9 ± 2	18.8 ± 1	8.2 ± 1	Theoretical
HE0058–3231	27.7 ± 2	68.3 ± 19	47.3 ± 4	28.9 ± 7	Theoretical
HE0203–4627	14.4 ± 2	41.5 ± 6	25.1 ± 4	17.3 ± 4	Theoretical
HE0248–3628	13.6 ± 0.5	62.7 ± 3	28.1 ± 3	31.1 ± 1	Theoretical
HE1349+0007	18.5 ± 1	51.6 ± 6	38.5 ± 8	23.2 ± 6	Theoretical
HE1409+0101	36.2 ± 2	203.8 ± 79	3.4 ± 0.4	3.6 ± 1	Theoretical
HE2147–3212	35.0 ± 4	85.4 ± 12	11.3 ± 2	5.6 ± 1	Semi-empirical
HE2202–2557	12.7 ± 1	31.1 ± 3	8.1 ± 2	3.6 ± 1	Theoretical
HE2340–4443	15.4 ± 1	50.4 ± 3	13.0 ± 1	15.2 ± 4	Theoretical
HE2349–3800	19.9 ± 1	35.7 ± 2	8.6 ± 1	4.5 ± 1	Semi-empirical
HE2352–4010	17.6 ± 0.3	147.6 ± 5	12.8 ± 1	26.8 ± 3	Semi-empirical

if FWHM(Hβ_{BC}) is really systematically larger than FWHM (CaT) and FWHM(O I λ8446), the Hβ emission associated with BC only may still preferentially come from regions closer to the central black hole than CaT and O I λ8446.

It is also interesting to compare the FWHM of O I λ8446 and CaT (bottom panel of Figure 8). At least to a first approximation, O I λ8446 and CaT show consistent FWHM values. The Persson data suggest that CaT is slightly systematically broader than O I λ8446. This effect is not seen in our data, however, which have much larger uncertainties. A small CaT and O I λ8446 FWHM difference may be explained in the context of the different emissivity of the two lines as a function of ionization parameter and density. If the two lines are not emitted in a coexistence region (Rodríguez-Ardila et al. 2002a; Matsuoka et al. 2005, 2007), they can be emitted in two regions with different physical conditions but which are kinematically coupled. Considerations of ionization parameter and density may support this possibility (discussed in Section 7.1).

6.4. Relation to Fe II

Photoionization models performed by Joly (1989) have shown that the relation between the ratios CaT/Hβ and Fe II λ4570/Hβ provides evidence of a common origin for CaT and Fe II λ4570: CaT/Hβ increases at high density and low temperature as does Fe II λ4570/Hβ (Joly 1987). Our sample follows the same trend found by Joly (Figure 9), with a Spearman correlation coefficient $\rho \approx 0.73$, yielding a negligible probability ($P < 10^{-4}$) that the correlation arises from statistical fluctuations. The correlation is consistent with the

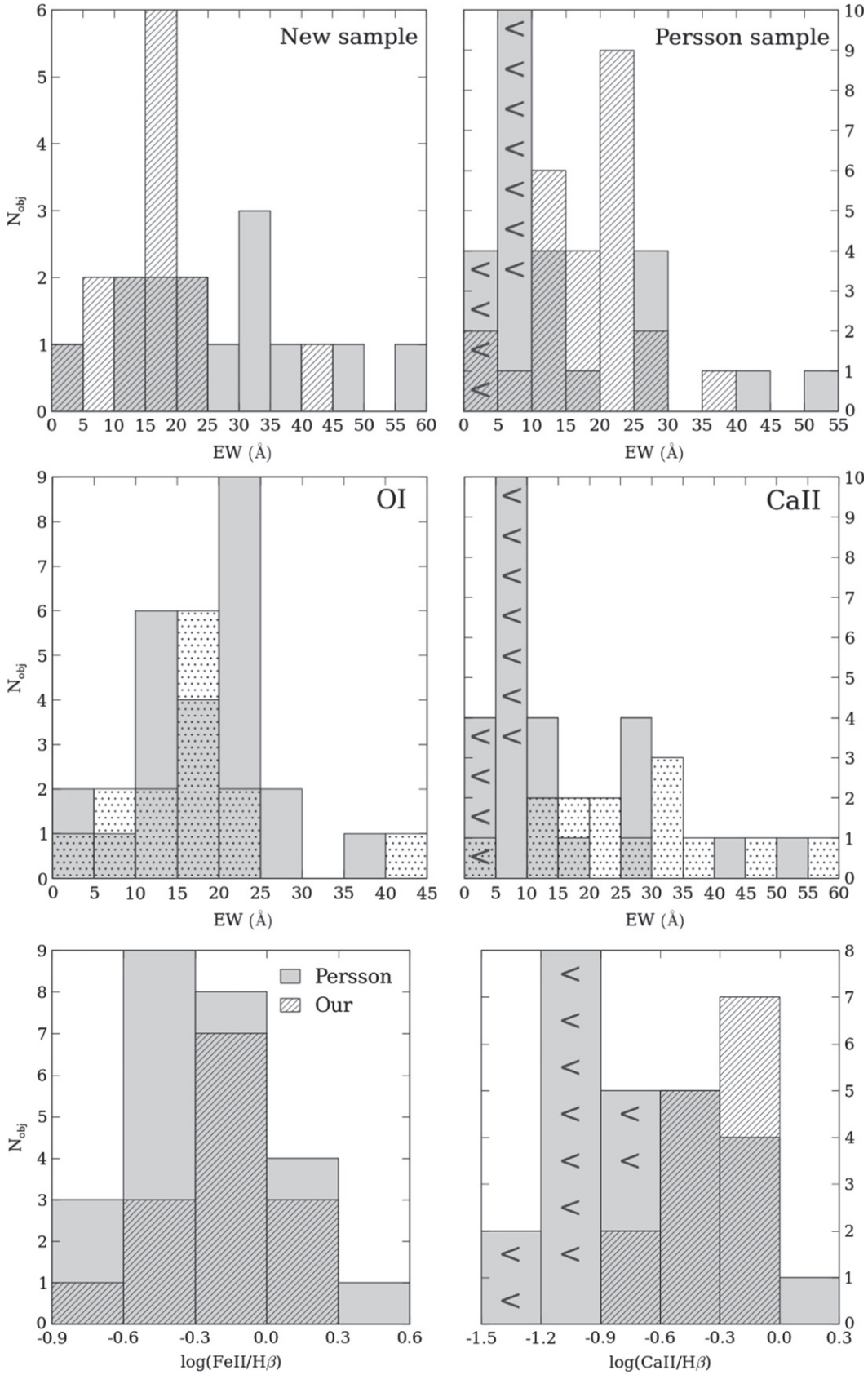

Figure 7. Top panels: histograms of W(O I) (hatched) and W(Ca II) (shaded) for our new ISAAC sample and Persson (1988). Arrowheads indicate upper limits. Middle panels: distributions of W(O I λ8446) (left) and W(Ca II) (right) in our new sample (dotted) and from Persson (1988; shaded). Bottom panel: distributions of Fe II λ4570/Hβ ($R_{\rm Fe\,II}$) and CaT/Hβ for our ISAAC sample (hatched) and Persson (1988; shaded).

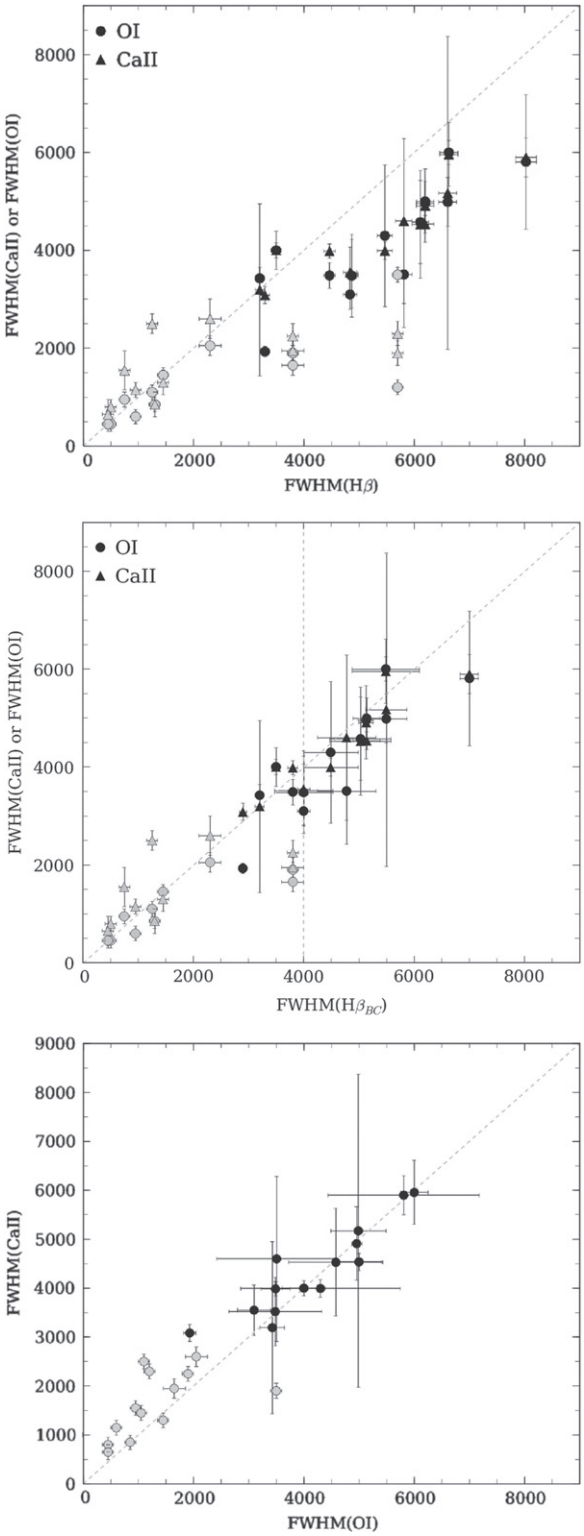

Figure 8. Top: comparison between the Ca II triplet, O I λ8446, and Hβ FWHMs, in km s^{-1}. Abscissa is the Hβ FWHM (full profile, i.e., BC +VBC), ordinate is the Ca II Triplet and OI λ8446 FWHM. Circles represents the O I data, while squares are Ca II triplet data. Black symbols are from our sample and gray symbols represent the Persson sample. The diagonal dashed line is the equality line. The vertical dashed line at 4000 km s^{-1} indicates the separation between Pop. A and B. Middle: same as above but for FWHM Hβ$_{BC}$. Bottom: FWHM(CaT) vs. FWHM(O I λ8446).

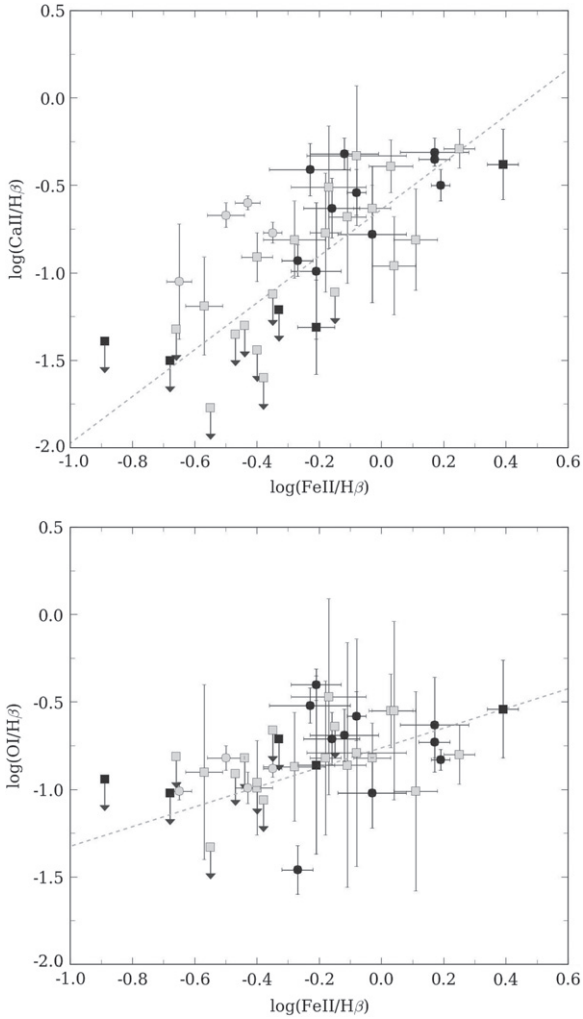

Figure 9. Top: relation between the observed ratios log(Fe II λ4570/Hβ) and log(CaT/Hβ). Circles indicate our sample, while squares indicate the Persson sample. Gray symbols indicate Pop A. sources, while black symbols indicate Pop. B sources. The arrows mark upper limits. Trendlines are represented by gray dashed lines. Bottom: same for log(O I λ8446/Hβ$_{BC}$) vs. log (Fe II λ4570/Hβ$_{BC}$).

idea that Fe II λ4570 and CaT are both emitted in a similar region, since the two lines are expected to be emitted under very similar physical conditions. If not, a hidden variable (metallicity or even orientation: Dultzin-Hacyan et al. 1999) could give rise to the observed correlation.

A least-squares fit including censored data provides the following relation: $\log(\mathrm{CaT/H}\beta) \approx (1.33 \pm 0.23)\log(\mathrm{Fe\ II}\ \lambda4570/\mathrm{H}\beta) - (0.63 \pm 0.07)$. The relation between O I λ8446/Hβ and Fe II λ4570/Hβ is, on the contrary, much more shallow, even if the slope is significantly different from 0: $\log(\mathrm{O\ I}\ \lambda8446/\mathrm{H}\beta) = (0.56 \pm 0.14)\log(\mathrm{Fe\ II}\ \lambda4570/\mathrm{H}\beta) - (0.76 \pm 0.05)$, implying that the systematic O I λ8446/Hβ change is a factor ≈3.5 for an order-of-magnitude increase in $R_{\mathrm{Fe\ II}}$.

6.5. Correlation with Redshift and Luminosity

Figure 10 shows that W(O I λ8446) does not correlate with luminosity over a range covering 4 dex in luminosity, as defined by our sample and Persson's data, with the addition of intermediate-luminosity sources from Matsuoka et al. (2007).

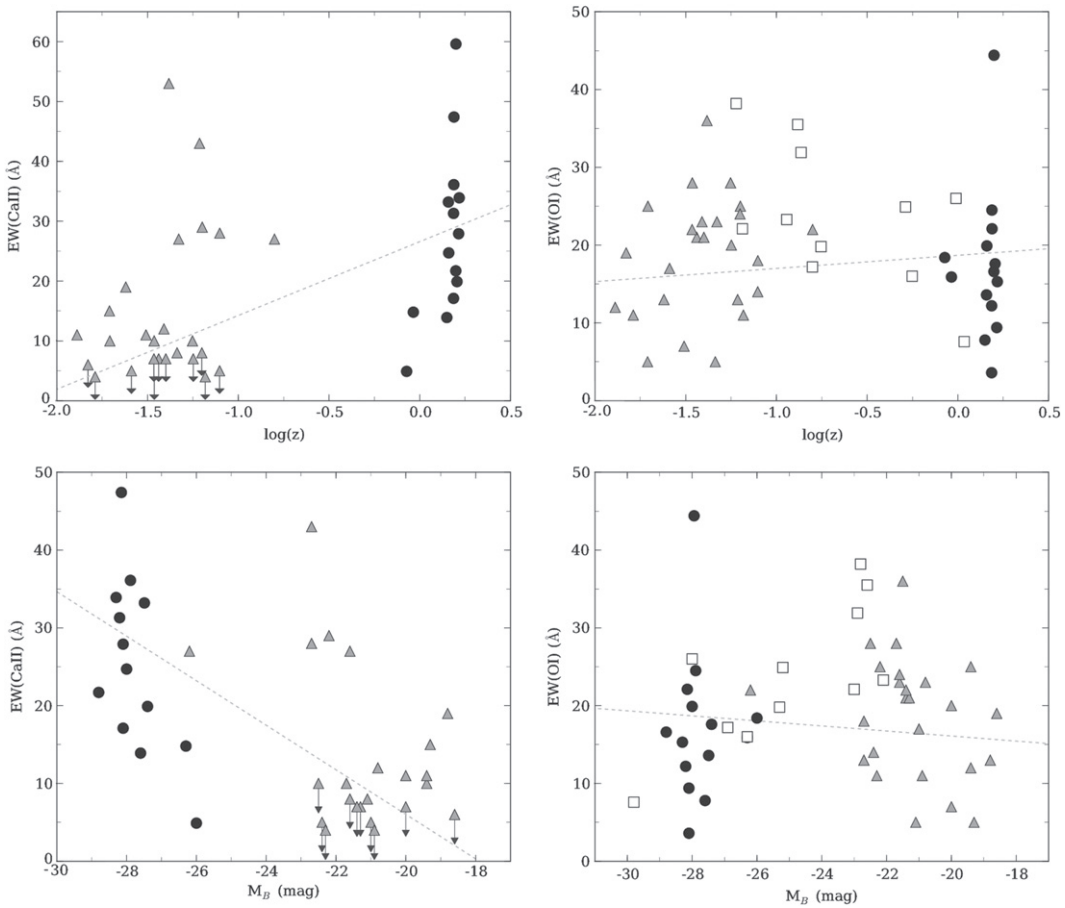

Figure 10. Equivalent width of CaT and O I λ8446 as a function of z (top) and absolute B magnitude (bottom). Filled circles: sample presented in this paper; triangles: data from Persson (1988); open squares: data from Matsuoka et al. (2007). Gray dashed lines are trendlines.

The present data do not support earlier claims of a low-ionization Baldwin effect in O I, either as a function of luminosity or as a function of redshift (i.e., an "evolutionary Baldwin effect").

The data shown in Figure 10 are statistically biased in terms of both z and L (i.e., they are not uniformly distributed over the covered range). In addition, there is a less-visible, difficult to quantify "Eddington bias" (see Sulentic et al. 2014 for a discussion on this topic): our high-z Pop. B sources may be those with the largest $L/L_{\rm Edd}$ possible for Pop. B. Therefore, great care should be taken when interpreting the bottom left panel of Figure 10 before claiming a correlation, even if the correlation coefficient is –0.564 with a probability $<10^{-4}$ of a chance correlation. If we accept this at face value, the trend between $M_{\rm B}$ and W(CaT) would imply an increase in the prominence of CaT with L and z. We see two possible explanations for this result, in addition to an intrinsic luminosity effect: (a) a larger ratio CaT/Fe II λ4570 in the high-L sample; (b) a systematic difference in the Fe II λ4570/Hβ distribution between our sample and the sample of Persson (1988).

The correlation between CaT/Hβ and Fe II λ4570/Hβ implies that strong CaT emission is associated with strong Fe II λ4570 emission. The bottom left panel of Figure 7 shows the $R_{\rm Fe\,II}$ distribution for our sample and Persson's. They are not significantly different according to generalized Wilcoxon's tests (also repeated without censored data). Therefore, the trend in Figure 10 cannot be ascribed to a systematic difference in

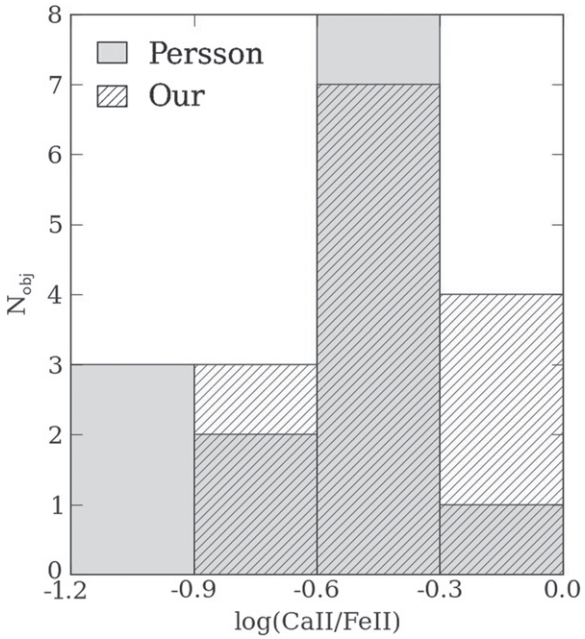

Figure 11. Distribution of CaT/Fe II λ4570 for the samples presented in this paper (hatched) and in Persson (1988; shaded).

$R_{\rm Fe\,II}$. The bottom right panel of Figure 7 shows the CaT/Hβ distributions. In this case, the same two sample tests yield a significant difference. Figure 11 shows the CaT/

Fe II λ4570 distributions (only for detected data) that are probably least affected by selection effects[7] and they are found to be significantly different with a confidence above the 2σ level: the CaT/Fe II λ4570 ratio average is larger by a factor ≈1.7 for the ISAAC sample. This effect can account at least in part for the L and z trends in Figure 10, and is a potentially important result that will be discussed in Sections 7.3 and 7.4, even if confirmation from a larger sample and a set of observations obtained with the same instrument including low- and high-z sources is needed.

7. DISCUSSION

7.1. Comparison With Photoionization Models

We computed photoionization models using the code Cloudy (Ferland et al. 1998, 2013) in order to constrain the physical conditions of the region where CaT and O I λ8446 are emitted. The simulations include a 371-level Fe II ion that allows some limited comparison with the observations of optical and IR Fe II emission. Simulations span the density range $7.00 < \log n_{\rm H} < 14.00\,{\rm cm}^{-3}$ and the ionization parameter range $-4.50 < \log U < 00.00$, in intervals of 0.25 dex assuming plane-parallel geometry. The spectral energy distribution of the ionizing continuum is that of Mathews & Ferland (1987) which is considered a standard for quasars. Open geometry, line thermal broadening, and solar metallicity are assumed. We consider column density values 10^{23} and $10^{25}\,{\rm cm}^{-2}$. Figure 12 shows isopleths of the predicted CaT/O I λ8446 ratio as a function of U and $n_{\rm H}$ for the two values of column density. Figure 13 shows the panel isopleths in the plane $(U, n_{\rm H})$ for CaT/Hβ, O I λ8446/Hβ, CaT/Pa9, and O I λ8446/Pa9, again for the two values of column density.

From a first comparison between the photoionization prediction at $Z = Z_{\odot}$ and the observed line ratios, we can draw the following preliminary conclusions.

1. The geometrical depth of the fully ionized zone does not exceed the geometrical depth of the gas slab in the case of $N_c = 10^{25}\,{\rm cm}^{-2}$. There is a depth range where the gas is only partially ionized, even at the highest U ($\log U \sim 0$). In other words, the ionizing photon flux is not able to make the cloud optically thin. In a photoionization context, O I λ8446 and especially CaT emission will be observed only if the emitting gas remains optically thick to the Lyman continuum. Therefore, in the high-ionization parameter area of the plane $(n_{\rm H}, U)$, we still have some emission of O I λ8446 and CaT that it is not predicted when N_c is smaller, $10^{23}\,{\rm cm}^{-2}$.
2. Constraints on the density of the emitting regions follow from maximum and minimum measured values of CaT/Hβ, O I λ8446/Hβ, CaT/Pa9, and O I λ8446/Pa9. Regardless of $N_{\rm c}$, the ratios involving CaT (when CaT emission is detected at a high significance) suggest that emission occurs only at relatively high density $\log n_{\rm H} \gtrsim 11.00$, with an upper limit to the ionization parameter $\log U \approx -1.5$, in agreement with the results of Matsuoka et al. (2007).
3. The median values of the CaT/Hβ (≈ −0.6) and CaT/O I (≈0.2) ratios do not favor the area in the plane $(U, n_{\rm H})$ at very low ionization and high density ($\log n_{\rm H} \gtrsim 12$, $\log U \lesssim -2.5$), unless density becomes $\log n_{\rm H} \sim 13$. In this region, significant emission of CaT—but not of O I λ8446—can occur.
4. The ratios of CaT and O I λ8446 normalized to Hβ and Pa9 look strikingly similar (Figure 13). Hβ and Pa9 are practically interchangeable. The upper half of Table 5 lists the logarithm of the observed flux ratios for Hβ and Pa9 (BC only),O I λ8446, and CaT.

The observed equivalent width of CaT can be ≈50 Å, and W (O I λ8446) $\lesssim$ 25 Å. These large equivalent widths are observed in both our sample and the Persson sample. Reaching values that high for CaT is possible in the framework of photoionization within the broad $n_{\rm H}$ lower limit and U upper limit set above. W(CaT) is strongly dependent on the column density in the area centered at $(n_{\rm H}, U) \approx (11.5, -2.5)$: the larger column density case yields an almost 10 fold increase in W (Ca II), while the effect is much lower for O I λ8446.

If we want to impose the conditions that O I λ8446 and CaT are emitted mainly within the same range of physical conditions, then a high metallicity ($5\,Z_{\odot}$) seems to be required in order to account for the largest observed W(O I λ8446) with a reasonable covering factor (≈0.2). Metallicity of solar or higher than solar is a very likely condition for HE sources. They are among the most luminous quasars known and there is a well-defined correlation between Z and luminosity (e.g., Shin et al. 2013). Among Pop. B sources, the HE quasars show large $R_{\rm Fe\,II}$. Therefore, strong CaT and O I λ8446 emitters (the values of Table 3 are loosely correlated) would benefit from large column density and high Z. We remark that the condition of high Z is needed to explain in particular the O I strength if we require that O I λ8446 and CaT are emitted under similar conditions. This might not necessarily be the case.

At variance with CaT, O I λ8446 can be emitted over a wide range of densities: $9.00 \lesssim \log n_{\rm H} \lesssim 12.00$. We interpret the difference in behavior as due to (1) the similarity of neutral hydrogen and oxygen ionization potentials (≈13.6 eV) and (2) the Bowen fluorescence mechanism, which is strongly influenced by the ionizing photon flux. The Bowen mechanism has indeed been found to be the major contributor to the O I intensity in most AGNs studied by Rodríguez-Ardila et al. (2002a) and Landt et al. (2008). Therefore O I λ8446 emission can originate in deep regions exposed to a large ionizing photon flux provided that the column density is high $N_c \sim 10^{23-25}\,{\rm cm}^{-2}$. These properties are consistent with those of VBLR seen in Pop. B sources (Marziani et al. 2010).

To frame these results for physical conditions in a broader scenario encompassing kinematics, we have to consider inferences that come from an analysis of internal line shifts and profile differences. A basic result is that the BLR can be separated into two main regions: one emitting mostly LILs and the other emitting HILs. In Pop. A sources, a blueshift and asymmetry (as in the prototypical HIL C4λ1549) indicate that the HILs are emitted within a partially obscured flow (Sulentic et al. 2007; Richards et al. 2011; Wang et al. 2011). Photoionization models further suggest that the HIL emitting region has a relatively low density ($n_{\rm H} \sim 10^{9}\,{\rm cm}^{-3}$), a column density of $10^{21-23}\,{\rm cm}^{-2}$, and a high ionization parameter, $U \sim 10^{-1}$, which is more than 10 times the value appropriate for LIL emission (Netzer 2013).

The hydrogen lines (typically Hβ) have been used as representative lines of the LILs. Photoionization models show

[7] There is no a priori reason why we should select sources with a biased distribution of CaT/Fe II λ4570 since we are able to measure the ratio CaT/Fe II λ4570 over a broad range of values (∼0.05–0.7) and we have undistinguishable $R_{\rm Fe\,II}$ distributions for the Persson and ISAAC sample.

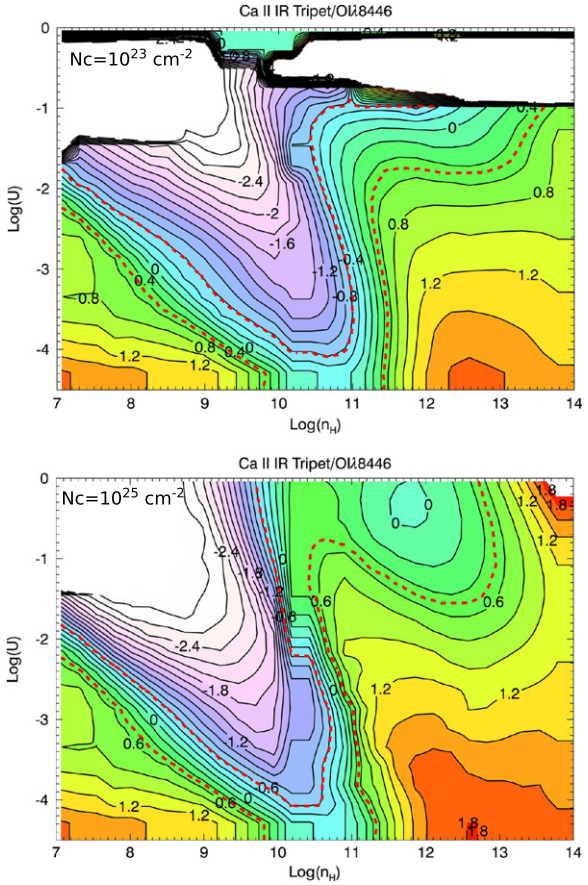

Figure 12. Isocontours of CLOUDY simulation results for line ratio log(CaT/O I λ8446). Abscissa is hydrogen density in cm^{-3}, ordinate is the ionization parameter, both in logarithmic scale. Top: models with N_c of 10^{23} cm^{-2}. Bottom: models with N_c of 10^{25} cm^{-2}. The dashed red line marks the maximum and the minimum value from the observations. All our measurements are inside this region.

that LIL emission is associated with a density that can be as high as $\sim 10^{11.5-12}$ cm^{-3}, column density $\gtrsim 10^{23}$ cm^{-2}, and a rather low-ionization parameter log $U \approx -2$ (Marziani et al. 2010; Netzer 2013). However, even under these conditions, it is not possible to reproduce the intensity of very low ionization lines, like the Fe II features (Wills et al. 1985). Fe II lines need a higher column density ($N_c \sim 10^{24}$ cm^{-2}) that makes possible an extended partially ionized zone at a relatively low electron temperature ($T \sim 8000$ K; Collin-Souffrin et al. 1980; Collin-Souffrin 1987; Joly 1987; Ferland & Persson 1989; Matsuoka et al. 2007).

In Pop. B the blueshifted component seems to be less prominent. The HILs are emitted closer to the central source than the LILs (Peterson & Wandel 1999), implying a radial stratification of the emitting region. The distinction of BC/VBC is the most simple parameterization of the ionization stratification, with VBC being associated with highly ionized (log $U \sim -0.1$), large column density gas (log $N_c \gtrsim 23$), probably with a broad range of density (Snedden & Gaskell 2007; Marziani et al. 2010).

7.2. A VBC for O I λ8446?

We observe a similarity between the O I λ8446 and Hβ profiles (see Landt et al. 2008). If we take into account the results of photoionization models, then it is reasonable to investigate the possibility that O I λ8446 shows significant VBC emission similar to redshifted VBC emission observed in Hβ of Pop. B sources.

In order to test the presence of VBC in O I λ8446, we added this component to the fits for Pop. B sources. The fits for HE0035–2853 and HE1349+0007 are shown in Figure 14. The results are basically the same with or without the inclusion of VBC. Even if the FWHM of O I λ8446 and CaT are the same using models with and without VBC, the flux values changed. The inclusion of VBC reduces the intensity in O I λ8446 and CaT by 10–30% and 20–60%, respectively. This reduction implies only slightly different physical conditions when the intensity ratios are entered into the (U, n_H) contour diagrams. The lower half of Table 5 reports values for the CaT/Hβ, O I λ8446/Hβ, CaT/Pa9, O I λ8446/Pa9, and CaT/O I λ8446 ratios including a VBC for O I λ8446. Comparing the ratios with and without VBC, we see that there is no difference within the errors. For example, if we only assume a BC, then the range of the ratio CaT/O I λ8446 is [–0.59, 0.53], while including the O I λ8446 VBC implies [–0.62, 0.40]. Therefore, the inclusion of an O I λ8446 VBC does not significantly modify inferences about the density in the CaT and O I λ8446 emitting region: log $n_H \gtrsim 11.00$ and $9.00 \lesssim$ log $n_H \lesssim 12.00$, respectively.

The fits carried out without an O I λ8446 VBC indicate that there is no empirical requirement for significant VBC emission to obtain acceptable residuals. However, the photoionization models indicate that some O I λ8446 VBC contribution could be present. Also, the shape of the CaT + O I λ8446 blend bears a striking similarity to the Hβ profile in sources where the Hβ VBC is unambiguously present. The S/N of our data is not high enough to constrain any VBC emission in χ_ν^2 solutions. We consequently decided to consider a model involving a single Gaussian for O I λ8446 with eventual consideration for a possible VBC contribution.

7.3. Ca II Triplet and O I λ8446 (and Fe II) in the 4DE1 Context

Several important aspects emerge from the previous analysis: in the context of a photoionized gas, CaT can mainly be emitted in a low-ionization, dense medium of high column density. In the last few decades, there has been considerable progress in modeling Fe II emission in the context of photoionization. As mentioned, the same physical conditions suited for Ca II are also suggested for Fe II emission. The relation between $R_{Fe\,II}$ and Ca II/Hβ implies that the same physical mechanisms should be operating in the emission of both Fe II and Ca II.

The present study confirms that Ca II and Fe II emissions are correlated even in very high luminosity objects (Figure 9). Figure 8 shows that our sample and the low-luminosity sample of Persson partly overlap and smoothly merge. This is further confirmation that 4DE1 correlations involving low-ionization emission line ratios are also orthogonal to luminosity.

The 4DE1 sequence is, at least in part, a sequence of increasing optical Fe II prominence (Marziani et al. 2009 and references therein), and our sample contains mainly Pop. B sources; the Ca II detection confirms that a dense, low-ionization region also has to be present in Pop. B sources. Therefore, the change along the 4DE1 sequence should be ascribed to a systematic variation contribution of a low-ionization region: from a low contribution to Fe II and

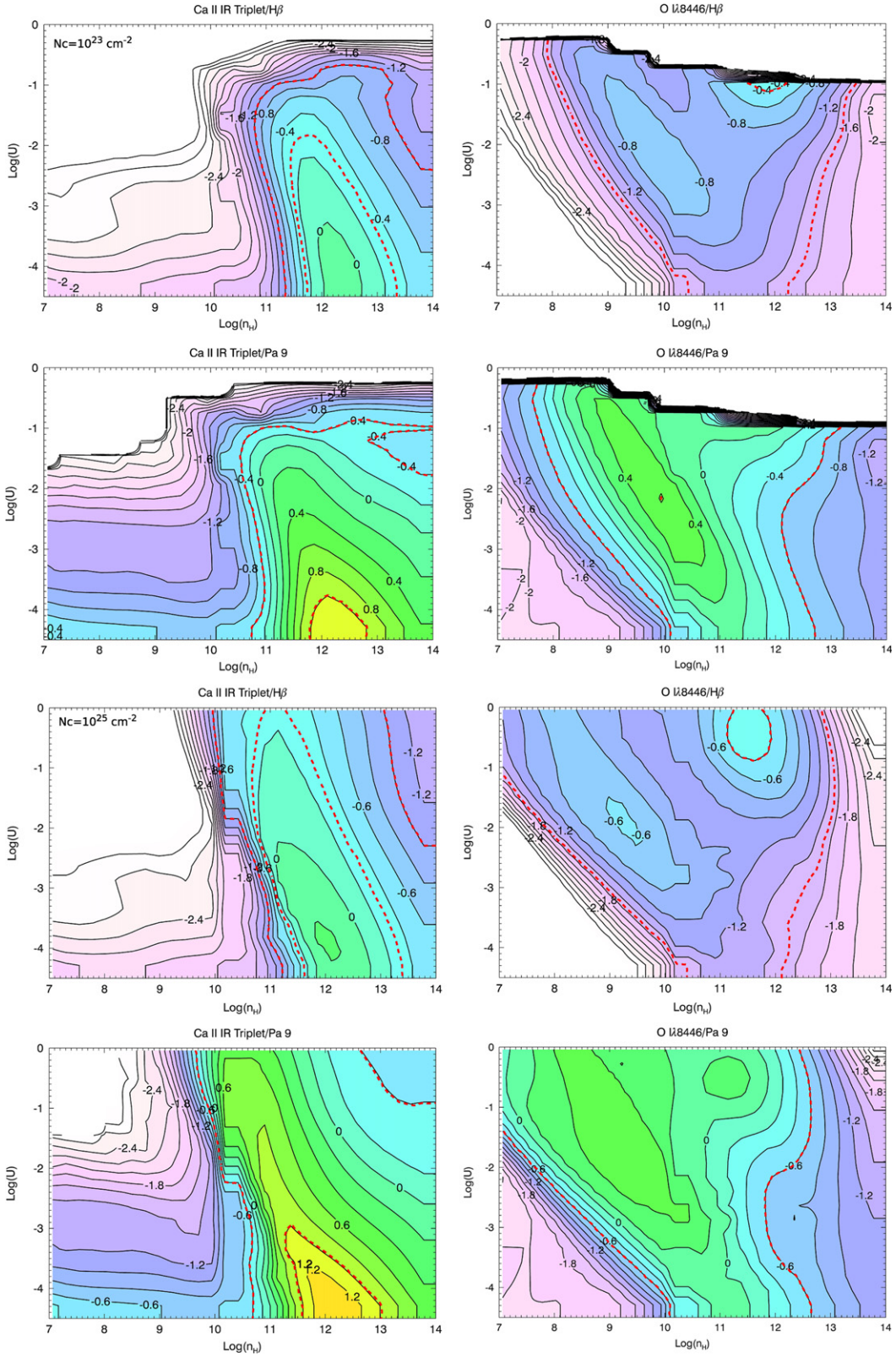

Figure 13. Isocontours of CLOUDY simulation results for line ratios $\log(\mathrm{CaT/H}\beta)$, $\log(\mathrm{O\,I}\ \lambda8446/\mathrm{H}\beta)$, $\log(\mathrm{CaT/Pa9})$, and $\log(\mathrm{O\,I}\ \lambda8446/\mathrm{Pa9})$. Abscissa is hydrogen density in cm^{-3}, ordinate is the ionization parameter, both in logarithmic scale. Top: model with column density $N_c = 10^{23}\ \mathrm{cm}^{-2}$. Bottom: model with $N_c = 10^{25}\ \mathrm{cm}^{-2}$.

Ca II emission in extreme Pop. B sources, to a maximum contribution in extreme Pop. A sources (Negrete et al. 2012).

Recent results for the reverberation time lag measured for three Seyfert 1 galaxies (NGC 4593, Mrk 1511, and Akn 564) strongly support the conclusion that Fe II emission originates in photoionized gas located predominantly in the outer portion of BLR (Shapovalova et al. 2012; Barth et al. 2013). Our analysis indicates that CaT and O I λ8446 can be interpreted as emission from photoionizated gas, with CaT strongly favored at low ionization and high density. The conditions we suggest are

Table 5
Observed Flux Ratios for the BC of Hβ, Pa9, O I λ8446, and Ca II Triplet

Object Name	log (CaT/Hβ)	log (O I/Hβ)	log (CaT/Pa9)	log (O I/Pa9)	log (CaT/O I)
No O I VBC					
HE0005–2355	−0.78	−1.02	0.11	−0.13	0.24
HE0035–2853	−0.35	−0.73	0.28	−0.09	0.38
HE0043–2300	−0.67	−0.82	0.35	0.20	0.16
HE0048–2804	−0.99	−0.40	−0.39	0.20	−0.59
HE0058–3231	−0.41	−0.52	−0.06	−0.17	0.11
HE0203–4627	−0.32	−0.69	0.86	0.48	0.37
HE0248–3628	−0.60	−0.99	0.46	0.07	0.39
HE1349+0007	−0.63	−0.71	0.45	0.37	0.08
HE1409+0101	−0.50	−0.83	0.49	0.16	0.33
HE2147–3212	−0.31	−0.63	0.97	0.66	0.32
HE2202–2557	−0.93	−1.46	−0.07	−0.60	0.53
HE2340–4443	−1.05	−1.01	0.37	0.41	−0.04
HE2349–3800	−0.54	−0.58	0.49	0.45	0.04
HE2352–4010	−0.77	−0.88	0.35	0.24	0.11
O I VBC					
HE0005–2355	−0.94	−1.10	−0.05	−0.21	0.17
HE0035–2853	−0.58	−0.79	−0.02	−0.23	0.21
HE0043–2300	−0.67	−0.82	0.35	0.20	0.16
HE0048–2804	−1.14	−0.52	−0.52	0.10	−0.62
HE0058–3231	−0.74	−0.52	−0.40	−0.17	−0.22
HE0203–4627	−0.70	−0.75	0.37	0.32	0.05
HE0248–3628	−0.60	−0.99	0.46	0.07	0.39
HE1349+0007	−0.74	−0.89	0.34	0.19	0.15
HE1409+0101	−0.67	−0.96	0.36	0.08	0.29
HE2147–3212	−0.45	−0.71	0.83	0.57	0.26
HE2202–2557	−0.96	−1.36	−0.01	−0.41	0.40
HE2340–4443	−1.05	−1.01	0.37	0.41	−0.04
HE2349–3800	−0.70	−0.65	0.34	0.39	−0.05
HE2352–4010	−0.77	−0.88	0.35	0.24	0.11

similar to those identified for Fe II (Verner et al. 1999; Sigut & Pradhan 2003; Sigut et al. 2004; Bruhweiler & Verner 2008). Therefore, photoionization models are probably appropriate at least in moderate Fe II emitters. Refinements in modeling Fe II emission are needed to reconcile observations with theory, in order to reproduce the observed multiplet ratios and especially $\mathrm{Fe\,II_{UV}/Fe\,II_{opt}}$ (Sameshima et al. 2011).

Can the strongest Fe II emitters also be explained in a pure photoionization scheme? According to Collin-Souffrin (1986) and Joly (1987), a different source of heating is needed. The strongest Fe II emitters show continuity with fainter Fe II emitters in the 4DE1 sequence (Zamfir et al. 2010; Marziani & Sulentic 2012). By Occam's razor, invoking an additional mechanism should be avoided if no discontinuity is observed. By virtue of the correlation in Figure 9, a strong CaT emitter should be also strong Fe II emitters. If log CaT/Hβ ≈ −0.3, then we expect $R_{\mathrm{Fe\,II}} \approx 2$. The results of this paper indicate that the strongest observed CaT can be accounted for in a photoionization scenario, suggesting that strong Fe II emitters with $R_{\mathrm{Fe\,II}} \lesssim 2$ could also be explained by photoionization if CaT is a valid tracer of the Fe II emitting gas.

7.4. Implications for Star Formation

We pointed out (Section 6.5) a possible increase of W(CaT) with luminosity. This trend is prone to selection effects and should be viewed with caution. The CaT/Fe II λ4570 ratio is, on average, a factor of ≈1.7 larger in our sample than in Persson (1988). We regard CaT/Fe II λ4570 as a reliable measurement. It is unlikely that the difference stems from different analysis techniques. In fact, our measures are corrected for Fe II and high-order Paschen lines while Persson's were not. There could be several other factors affecting the CaT/Fe II λ4570 ratio, for example, effects associated with microturbulence and spectral energy distribution (Verner et al. 2003; Matsuoka et al. 2007). The effect of microturbulence on UV Fe II could be especially relevant if v_{turb} is as high as 100 km s^{-1}. Its effect on the optical Fe II emission could be much less, as tested by CLOUDY simulations for plausible values of U and n_{H} (−2.5, 12.00). The possibility of a softer SED has been checked by comparing a simulation with the Mathews & Ferland (1987) SED and with the NLSy1 SED of Marziani & Sulentic (2014). The effect of a softer X-ray spectrum is relatively modest, yielding a ≈25% decrease in the CaT/Fe II λ4570 ratio at a fixed U. This last effect may influence our data since Persson sources are mainly NLSy1, while our sample includes mainly Pop. B but is unable to fully account for the difference between the two samples.

If (1) CaT/Fe II λ4570 traces the calcium abundance as well as the abundance ratio of calcium and iron and (2) if the calcium abundance scales with other α elements, then a CaT/Fe II λ4570 increase at higher z could be associated with circumnuclear star formation or host galaxy evolution because the ratio [α/Fe] represents a sort of "chemical clock" with [α/Fe] being higher at earlier cosmic times (e.g., Matteucci 2012 and references therein). An overabundance, relative to Fe, of α elements such as calcium is expected if there has been enrichment from a recent burst of star formation: the α elements are produced through core collapse supernovae on timescales $\lesssim 3 \times 10^7$ yr, while iron is due to Type Ia supernovæ associated with much longer timescales, $\sim 10^9$ yr (Wyse & Gilmore 1988; Matteucci 2003). The sources with largest W(CaT) in the Persson (1988) sample (e.g., the ultra-luminous IR galaxy Mrk 231; Braito et al. 2004) are also those known to be associated with strong star formation and large $R_{\mathrm{Fe\,II}}$. These low-z sources, however, show a CaT/Fe II λ4570 ratio that is close to the average of the low-z sample. In the simplest scenario of a circumnuclear burst of star formation, an enhanced CaT/Fe II λ4570 ratio may imply that star formation in intermediate-z quasars has been sustained over a shorter timescale than in the case of the large $R_{\mathrm{Fe\,II}}$ sources in the low-z sample or, more likely, that massive stars are continuously forming. It is generally accepted that black hole growth and star formation are closely related (e.g., Sani et al. 2010; Kormendy & Ho 2013, for a review). Therefore, the higher CaT/Fe II λ4570 ratio observed in the ISAAC sample could possibly reflect the coevolution of the black hole and host galaxy (in the framework of massive black hole formation and bulge growth after a wet merger) that is expected to occur at intermediate and high z and to ultimately power the most luminous quasars.

7.5. A Possible Geometry of the BLR

The narrower line width of Fe II and Mg II λ2800 indicates that the distance from the central continuum source could be larger for these lines than for the Balmer lines (Sulentic et al. 2006; Marziani et al. 2013b) if the velocity field associated with line broadening is predominantly virial. According to the physical condition inference from CaT, a natural site of

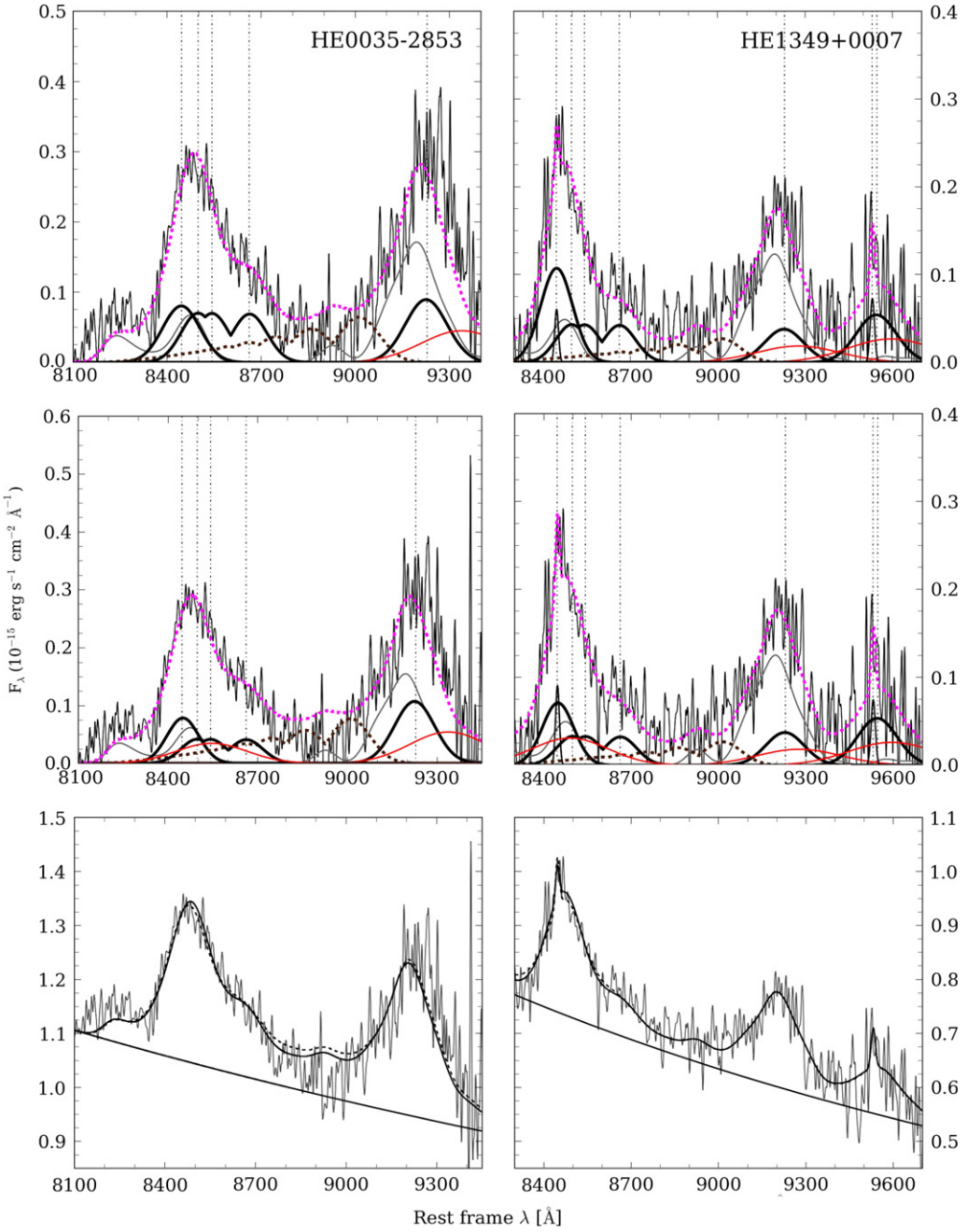

Figure 14. Fits with and without O I λ8446 VBC O I λ8446. The upper panels show the model with only BC. The middle panels present model fits with O I λ8446 VBC. The meaning of the line coding is the same of Figure 3. In the bottom panels, the continuous lines mark the model with O I λ8446 BC only, while the dashed lines mark the model with BC+VBC. We do not observe a significant difference.

emission for LILs is the accretion disk that provides a high column density environment (Collin-Souffrin 1987; Collin-Souffrin et al. 1988; Ferland & Persson 1989). Physical conditions may not be strictly the same for O I and Ca II emission. O I is more likely emitted in a region with physical conditions similar to Hβ (Section 7.1).

For example, we may envision a plane-parallel distribution of BLR clouds above and below the accretion disk. In this configuration, the cloud dynamics is dominated by gravity and the emitting gas motion is virialized. Some of these clouds might be at the same distance from the ionization source as some accretion disk regions, and therefore they may share the same dynamics.

The Ca II and O I emitting regions should share a similar ionization status since the two ions have similar ionization potentials. This (along with the kinematical similarity) leads to the interpretation that CaT and O I λ8446 are emitted from physically overlapping gas. However, they do not necessarily share exactly the same density and ionization status. From Figure 13, we see that the observed O I λ8446/Hβ ratio leads to poor constraints on $n_{\rm H}$ and U. If r is similar because of similar kinematics, then there is a large range in $n_{\rm H}$ and U that will be consistent with the observed O I λ8446/Hβ, keeping the ionizing photon flux the same for the two lines. This indicates that O I λ8446 and CaT may have similar FWHM even if they are emitted in somewhat different conditions. A possible model

involves an illuminated accretion disk in vertical hydrostatic equilibrium at each radius: Ca II may arise with higher efficiency than O I λ8446 from the deepest regions of the disk.

The geometry of BLR is likely dependent on the source location in the 4DE1 sequence. The 4DE1 is probably a sequence of the Eddington ratio, which decreases from Pop. A to Pop. B (Marziani et al. 2001). Non-gravitational forces such as radiation pressure are expected to be operating at maximum strength in extreme Pop. A sources (Marziani et al. 2008; Netzer & Marziani 2010; Negrete et al. 2013). Among Pop. B sources, we frequently observe strong redward asymmetries in the Hβ profiles, and they are very prominent in the spectra of our sources. The physical origin of these features is unclear (e.g., Punsly & Zhang 2010) and may be associated with a non-Doppler process. If redward asymmetries are associated with non-virial gas motions, then they may be seen as perturbations whose amplitude increases toward the line base of the Hβ profile, and thus toward the central continuum source. In the profile interpretation we adopt, we isolate a VBC in Hβ profiles that should represent this innermost part of the Hydrogen emitting region, the VBLR. The VBLR cannot emit Fe II or Ca II because the ionization level is too high.

As mentioned, however, hydrogen and oxygen have very similar ionization potentials but not necessarily the same ionization status, and O I λ8446 and Hβ could both be produced in an inner region exposed to a strong radiation field. Some O I λ8446 emission could be associated with VBLR. O I λ8446 emission could also be favored in an accretion disk plus wind scenario if the innermost regions of line emission are the densest and of highest optical depth (Flohic et al. 2012). The wind/disk scenario is also consistent with the idea of a mostly virial BLR for Pop. B in which an ionization gradient with distance is responsible for differences in line profiles and differences in response times found by reverberation mapping (the BC/VBC can be seen as a crude phenomenological model of such an ionization gradient). It remains to be seen how much O I λ8446 can be produced in the VBLR. Theoretical profiles for the different lines will be computed in a companion paper in order to ascertain how strong an O I λ8446 VBC might be.

8. CONCLUSION

We have analyzed a set of Ca II IR triplet + O I λ8446 observations for a sample of high-z luminous quasars and reported the detection of CaT emission in all sources with the exception of two. We carried out multicomponent fits that included detailed modeling of all emission features—most notably Fe II and high-order Paschen lines—in the range 8000–9500 Å. The fits allowed us to retrieve accurate line widths and fluxes of CaT and O I λ8446. The new measurements indicate that Ca II and optical Fe II emission are likely closely related. A possible systematic difference in the CaT/Fe II λ4570 ratio (which may also account for an apparent correlation of W(CaT) with z and L) has been found and indicates that recent star formation may be driving gas enrichment in the intermediate z-sample.

We present a preliminary interpretation of our measurements within a photoionization context. Photoionization models show that Ca II triplet and O I λ8446 can be emitted in regions with similar physical conditions, although there is a range of ionization parameter and density where only O I λ8446 emission is possible and CaT emission is negligible. We propose a scenario where the geometry of the BLR consists of plane parallel distributions of clouds above and below an accretion disk. In this configuration, cloud dynamics is dominated by gravity. Some of these clouds could be at the same distance from the ionization source as high-density regions within the accretion disk. The clouds and the emitting regions of the disk would share the same dynamics (same FWHM) but differ in physical conditions. Much CaT emission could come from the disk, while O I λ8446 could come from less dense gas located, however, at the same distance.

In this paper, we have followed a predominantly empirical approach with a detailed description of data analysis. In a companion paper, we will present additional data along with a study of the ionization mechanism associated with a Ca II triplet and O I λ8446 emission.

The authors thank the reviewer for the useful comments to improve this manuscript. D. D. acknowledges support from grant IN107313, PAPIIT UNAM. M. L. M.-A. acknowledges support from a CONACYT scholarship.

APPENDIX A
NOTES ON INDIVIDUAL SOURCES

HE0005–2355—CaT and O I λ8446 are completely blended. This is the source where Pa7 is detected. Emission on the red side of the Ca II triplet cannot be attributed to high-order Paschen lines because the decrease in intensity should be exponential and this is not observed. [S III] λ9531 is clearly seen.

HE0035–2853—One of the highest S/N spectra. The similarity between Hβ and the O I λ8446 + CaT blend is remarkable. We see significant Fe II emission which is also strong in the optical region. There is a clear asymmetry in the Pa9 + Fe II blend at ∼9000 Å due to Fe II. We can also see Fe II on the blue side of O I λ8446. It is underestimated in both theoretical and semi-empirical Fe II templates.

HE0043–2300—The contribution of NIR Fe II emission is weak (optical Fe II is also weak). The whole emission feature at ∼9200 Å is therefore likely to be Pa9. Although the spectrum is rather noisy, we can detect high-order Paschen lines (specially Pa10 and Pa11). Some excess emission on the blue side of O I λ8446 could not be reproduced.

HE0048–2804—This quasar shows the weakest CaT emission, if any. The blend fit is dominated by O I λ8446. Emission on the blend red side is well fit by high-order Paschen lines. Although Fe II is weak in the optical spectrum, it is reasonably strong in the NIR. Fe II contributes ∼70% of the observed flux in the bump at ∼9200 Å. Another interesting feature involves the prominent rise in intensity at ∼8200 Å which may be the beginning of the Paschen continuum. An I-band magnitude value is reported in the USNO-B Catalog (Monet et al. 2003), originating from photographic data taken ∼20 yr ago. If we normalize the Hβ spectrum to the USNO-B I magnitude, then we get a significant continuum flux increase of 25% which does not produce a qualitative change in our sample statistics. Due to the large period of time between photographic observations and our data, we prefer not to re-normalize the Hβ spectrum.

HE0058–3231—O I λ8446 is clearly detected but the CaT detection is uncertain. The higher-order Paschen line emission could not be reproduced, especially at ∼9000 Å. On the blue side of the spectrum, the presence of emission that decreases towards shorter wavelengths is evident and may hint at the presence of Paschen continuum.

HE0203–4627—O I λ8446 shows a blueshift of ∼−450 km s^{-1} similar to the one observed in the hydrogen lines. O I λ8446 and CaT are completely blended, showing a smooth profile but with a clear red asymmetry revealing the presence of CaT emission. The low intensity of Pa9 indicates that the contribution from higher-order Paschen lines is small. For instance, the contribution from Pa13 to the Ca II λ8662 profile is <10%. For this reason, the emission at ∼8900 Å cannot be ascribed to Paschen lines. The Fe II template underestimates the intensity of this feature. Fe II emission is nonetheless favored because Fe II is three times stronger than Pa9 at 9200 Å.

HE0248–3628—The high S/N of the spectrum allows us to detect Ca II λ8662 but does not allow us to distinguish Ca II λ8498 from λ8542. Hβ and NIR profiles show a strong similarity. Fe II emission is twice as strong as Pa9 and Pa10 and can partially account for the observed emission at 8900 Å. There is also a small feature at ∼9400 that has been identified with Fe II (Garcia-Rissmann et al. 2012) but that is not modeled by theoretical templates. Narrow [S III] λ9531 width is comparable to the narrow optical lines. We could not reproduce emission observed on the blue side of O I λ8446.

HE1349+0007—We found evidence for a narrow component in O I λ8446. For many years O I λ8446 was thought to be produced only in the broad line region (Grandi 1980). More recently, evidence was found that part of this line might arise in the narrow line region (Landt et al. 2008). Fe II (>50% of the flux in the Pa9 region) dominates the fit with higher-order Paschen lines making a minor contribution.

HE1409+0101—The optical spectrum shows prominent Fe II emission while the NIR spectrum may indicate less prominent Fe II emission. Some Paschen continuum emission may be present.

HE2147–3212—Low S/N spectrum. The only feature clearly observed is the O I λ8446 + CaT blend. Ca II λ8662 can be readily seen. We cannot fit the Pa9 line with good accuracy.

HE2202–2557—The only source spectrum requiring the subtraction of a host galaxy contribution. Host galaxy absorptions are clearly visible (especially the Ca II triplet). The stellar spectrum contributes 50% of the quasar continuum luminosity. After continuum subtraction, the O I λ8446 + CaT emission blend appears similar to the Hβ profile. O I λ7775 and O I λ8446 show the same width, with O I λ7775 stronger than O I λ8446. Emission between these lines can be well fit by the Paschen continuum. Higher-order Paschen lines are present but not unusually strong. O I λ8446 and CaT lines are weak with an equivalent width of a few angstroms. The reported flux and equivalent width errors in Table 3 are estimated in a manner consistent with the other sources. In the case of HE2202–2557, a large uncertainty is associated with continuum placement. Repeating the SPECFIT analysis indicates that ±50% may be a more realistic estimate of the flux and equivalent width uncertainty.

HE2340–4443—Modest S/N at 9200 Å prevents a reliable fit of the Pa9 line. High-order Paschen lines and Fe II measurements have a large uncertainty. O I λ8446 and CaT are completely blended and O I λ8446 dominates the fit. An I-band magnitude value is reported in the USNO–B Catalog (Monet et al. 2003). The I magnitude would change the flux scale by 40%. As for HE0048–2804, we prefer to keep the flux scale obtained from our calibration.

HE2349–3800—Low S/N makes it difficult to measure Pa9 and Fe II. The O I λ8446 + CaT blend is the only distinct feature. We can isolate the contribution of the Ca II λ8662 line. There is a bump on the blue side of O I that we cannot reproduce.

HE2352–4010—In this case, we distinguish the contribution of Ca II λ8662 as well as the other two lines of the triplet. We observe a bump on the blue side of O I λ8446 that cannot be modeled.

APPENDIX B
ERROR ESTIMATES

Synthetic Gaussian line profiles were built to estimate statistical errors involved in the line parameter measures. Since we are not dealing with isolated emission lines, we have to consider the effect of blending on error estimates. For the optical spectra, we considered the BC and VBC of Hβ. For the NIR spectra, we took into account that O I λ8446 and CaT are blended together. Model blends were constructed using O I λ8446 and the three individual components of CaT, to which we added Gaussian noise. Model profiles were built considering for the typical FWHM and equivalent width measured in our spectra. For Hβ BC, we assumed FWHM = 4800 km s^{-1}, W = 24, 40, 56, 70, and S/N = 20, 30, 40, 50, 60. For Hβ VBC, we considered FWHM = 10,500 km s^{-1}, W = 5, 10, 20, 30, 50, and the same S/N values. For O I λ8446, we considered FWHM = 4500 km s^{-1}, W = 10, 15, 20, 40, and S/N = 10, 20, 30, 40, 55. For CaT FWHM = 4300 km s^{-1}, W = 10, 20, 30, 50, 60 (sum of the three lines), and the same S/N values. In this way, we were able to build blended spectra with profiles similar to the ones seen in the real data of each quasars.

Let p_0 be a blended profile with a given FWHM and W to which noise has been added. Around it, a set of profiles $p_{0,ij}$ was built: (1) changing FWHM and keeping the flux and peak of the line fixed, and then (2) changing flux (and W) but keeping FWHM fixed. $\chi^2_{\nu,ij}$ values were computed for a fixed noise level as a function of FWHM and flux. The original profile p_0 is associated with the minimum χ^2_ν, $\chi_{\nu,\min}$. Errors are set through the ratio $F_{ij}=\chi^2_{\nu,ij}/\chi^2_{\nu,\min}$, and precisely by values of F_{ij} that correspond to the probability ≈0.32 (1σ confidence level) of reaching a $\chi^2_{\nu,ij}$ value because of statistical errors (i.e., associated with noise). Values of F_{ij} are computed for the degrees of freedom set by the number pixels in wavelength covered by the lines, minus the number of parameters appearing in the line model. The F_{ij} values provide confidence intervals as a function of FWHM, W, and S/N that define our uncertainty range. The FWHM error was taken from models where the FWHM varies and the peak of the line is fixed. Flux can be written as the product of FWHM times peak intensity. Error propagation on FWHM and peak intensity yields the total error on flux. The left panel of Figure 15 shows an example of blended synthetic profiles with FWHM(O I) = 4500 km s^{-1}, FWHM (Ca II) = 4300 km s^{-1}, W(O I) = 20 Å, W(CaT) = 20, and S/N = 20. The right panel shows the uncertainty range on FWHM and flux estimated from the appropriate F_{ij} value. The parameter $F = \chi^2_\nu/\chi^2_{\nu,\min}$ is shown in Figure 15 as a function of FWHM and the intensity of CaT and O I λ8446. $F \approx 1.03$ provides 1σ confidence ranges on the parameters. This is basically the classical χ^2_ν technique for error estimates described by Bevington & Robinson (2003) and by Press et al. (1995).

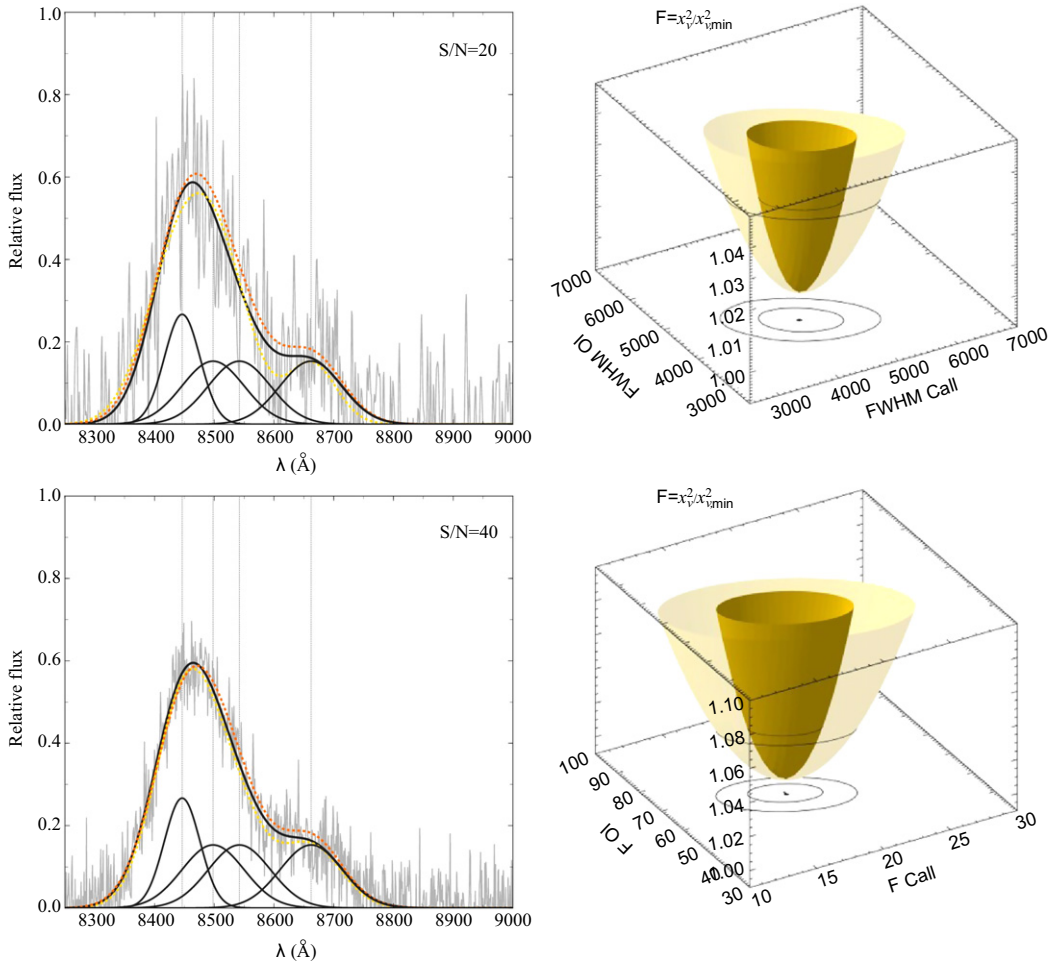

Figure 15. In the left panels we show the synthetic profiles for the blend O I λ8446 + CaT with FWHM(O I λ8446) = 4500 km s^{-1}, FWHM(Ca II) = 4300 km s^{-1}, W (O I λ8446) = 20 Å, W(Ca II) = 20, and S/N = 20, 40 (top and bottom, respectively). The dark line marks the model with the minimuum χ_ν^2, while the dashed line in color indicates the model at 1σ for FWHM and Flux (yellow and orange). The vertical dashed lines are the rest-frame for O I λ8446 and the Ca II triplet. In the right panels, the behavior of the F statistics is shown for the two different S/N values (pale: S/N = 20, dark S/N = 40). Contour lines (traced on the 3D paraboloids and on the xy plane) trace the 1σ confidence ranges on FWHM and flux reached for $F \approx 1.03$.

We also tested the effect of Ca II+O I blending with Monte Carlo simulations that allowed us to simultaneously fit flux and FWHM. The cases studied for the χ_ν^2 analysis were all repeated for different values of S/N. The Monte Carlo simulations involved the repetition of the blend fits for a large number of trials (≈1500 for each case) with different realizations of Gaussian noise patterns. The uncertainty on line parameters was then retrieved by the distribution of the measurements obtained changing the random noise patterns. We found that the errors are correlated with the ones estimated through the χ_ν^2 analysis but are significantly smaller, between a factor 1.3–1.5 and a factor $\gtrsim$2 for the flux of CaT. The lower errors can be understood by considering the nature of the Monte Carlo Method and by the fact that we are dealing with spectra whose S/N is relatively high, $\gtrsim$20 except for one case. In these conditions, the fitting routine converges to values close to the "true" ones, i.e., the starting values in absence of noise, yielding a rather peaked parameter distribution for different noise realizations.

In addition to Gaussian noise, another relevant source of error is continuum placement. To estimate its effect on flux, we considered a continuum intensity displacement of ±1σ with respect to the best fit. The W uncertainty was then estimated by propagating the errors for continuum and flux following the definition of W.

The uncertainty due to the inclusion of the Fe II template has been estimated through Monte Carlo simulations considering all components assumed to be present in the whole spectral range 8000–9900 Å. The flux and width assumed for each line are the ones reported in Tables 2 and 3, i.e., the ones measured on the observed spectra. We run two cases for each object in which the fitting routine (1) considers only one template as listed in Table 4, and (2) is left free to choose between the two different templates (theoretical or semiempirical). The ratio between the errors found for case 2 and case 1 gives us the uncertainty added by Fe II over the uncertainty associated with other components. We multiplied χ_ν^2 uncertainties by this ratio (always $\gtrsim$1) to include the effect associated with the Fe II template. The uncertainty increase ranges from a median of ≈10% to a maximum ≈50%. The effect depends on S/N and W and, in the Monte Carlo simulation context, should be ascribed to the inability of the fitting routine to identify which template is the best. The uncertainties computed with and without the effect of the Fe II template are reported in Tables 2 and 3. Figures 8 and 9 error bars include Fe II template uncertainty.

REFERENCES

Ammons, S. M., Robinson, S. E., Strader, J., et al. 2006, ApJ, 638, 1004
Barth, A. J., Pancoast, A., Bennert, V. N., et al. 2013, ApJ, 769, 128
Bentz, M. C., Denney, K. D., Grier, C. J., et al. 2013, ApJ, 767, 149
Bevington, P. R., & Robinson, D. K. 2003, Data Reduction and Error Analysis for the Physical Sciences (3rd ed.; Boston, MA: McGraw-Hill)
Boroson, T. A. 2002, ApJ, 565, 78
Boroson, T. A., & Green, R. F. 1992, ApJS, 80, 109
Braito, V., Della Ceca, R., Piconcelli, E., et al. 2004, A&A, 420, 79
Bressan, A., Granato, G. L., & Silva, L. 1998, A&A, 332, 135
Bressan, A., Marigo, P., Girardi, L., et al. 2012, MNRAS, 427, 127
Bruhweiler, F., & Verner, E. 2008, ApJ, 675, 83
Cenarro, A. J., Gorgas, J., Vazdekis, A., Cardiel, N., & Peletier, R. F. 2003, MNRAS, 339, L12
Collin-Souffrin, S. 1986, A&A, 166, 115
Collin-Souffrin, S. 1987, A&A, 179, 60
Collin-Souffrin, S., Dyson, J. E., McDowell, J. C., & Perry, J. J. 1988, MNRAS, 232, 539
Collin-Souffrin, S., Joly, M., Dumont, S., & Heidmann, N. 1980, A&A, 83, 190
Drake, A. J., Djorgovski, S. G., Mahabal, A., et al. 2009, ApJ, 696, 870
Dultzin-Hacyan, D., Taniguchi, Y., & Uranga, L. 1999, in ASP Conf. Series, Vol. 175, Structure and Kinematics of Quasar Broad Line Regions, ed. C. M. Gaskell, et al. (San Francisco, CA: ASP), 303
Falomo, R., Kotilainen, J. K., Pagani, C., Scarpa, R., & Treves, A. 2004, ApJ, 604, 495
Ferland, G. J., & Persson, S. E. 1989, ApJ, 347, 656
Ferland, G. J., Korista, K. T., Verner, D. A., et al. 1998, PASP, 110, 761
Ferland, G. J., Porter, R. L., van Hoof, P. A. M., et al. 2013, RMxAA, 49, 137
Flohic, H. M. L. G., Eracleous, M., & Bogdanović, T. 2012, ApJ, 753, 133
Floyd, D. J. E., Dunlop, J. S., Kukula, M. J., et al. 2013, MNRAS, 429, 2
Garcia-Rissmann, A., Rodríguez-Ardila, A., Sigut, T. A. A., & Pradhan, A. K. 2012, ApJ, 751, 7
Grandi, S. A. 1980, ApJ, 238, 10
Joly, M. 1987, A&A, 184, 33
Joly, M. 1989, A&A, 208, 47
Korista, K. T., & Goad, M. R. 2001, ApJ, 553, 695
Kormendy, J., & Ho, L. C. 2013, ARA&A, 51, 511
Kotilainen, J. K., Falomo, R., Labita, M., Treves, A., & Uslenghi, M. 2007, ApJ, 660, 1039
Kriss, G. 1994, adass, 3, 437
Kuehn, C. A., Baldwin, J. A., Peterson, B. M., & Korista, K. T. 2008, ApJ, 673, 69
Kukula, M. J., Dunlop, J. S., McLure, R. J., et al. 2001, MNRAS, 326, 1533
Landt, H., Bentz, M. C., Ward, M. J., et al. 2008, ApJS, 174, 282
Landt, H., Elvis, M., Ward, M. J., et al. 2011, MNRAS, 414, 218
Magorrian, J., Tremaine, S., Richstone, D., et al. 1998, AJ, 115, 2285
Malkan, M. A. 1983, ApJ, 268, 582
Malkan, M. A., & Sargent, W. L. W. 1982, ApJ, 254, 22
Marziani, P., Martinez-Aldama, M. L., Dultzin, D., & Sulentic, J. 2013a, ARev, 8, 4
Marziani, P., & Sulentic, J. W. 2012, ARev, 7, 33
Marziani, P., & Sulentic, J. W. 2014, MNRAS, 442, 1211
Marziani, P., Sulentic, J. W., & Dultzin, D. 2008, RMxAA, 32, 69
Marziani, P., Sulentic, J. W., Negrete, C. A., et al. 2010, MNRAS, 409, 1033
Marziani, P., Sulentic, J. W., Plauchu-Frayn, I., & del Olmo, A. 2013b, A&A, 555, A89
Marziani, P., Sulentic, J. W., Stirpe, G. M., Zamfir, S., & Calvani, M. 2009, A&A, 495, 83
Marziani, P., Sulentic, J. W., Zamanov, R., et al. 2003a, ApJS, 145, 199
Marziani, P., Sulentic, J. W., Zwitter, T., Dultzin-Hacyan, D., & Calvani, M. 2001, ApJ, 558, 553
Marziani, P., Zamanov, R. K., Sulentic, J. W., & Calvani, M. 2003b, MNRAS, 345, 1133
Mathews, W. G., & Ferland, G. J. 1987, ApJ, 323, 456
Matsuoka, Y., Oyabu, S., Tsuzuki, Y., & Kawara, K. 2007, ApJ, 663, 781
Matsuoka, Y., Oyabu, S., Tsuzuki, Y., Kawara, K., & Yoshii, Y. 2005, PASJ, 57, 563
Matsuoka, Y., Peterson, B. A., Oyabu, S., et al. 2008, ApJ, 685, 767
Matteucci, F. 2003, Ap&SS, 284, 539
Matteucci, F. 2012, Chemical Evolution of Galaxies (Berlin, Heidelberg: Springer)
Merloni, A., Bongiorno, A., Bolzonella, M., et al. 2010, ApJ, 708, 137
Monet, D. G., Levine, S. E., Canzian, B., et al. 2003, AJ, 125, 984
Moorwood, A., Cuby, J.-G., Biereichel, P., et al. 1998, Msngr, 94, 7
Negrete, C. A., Dultzin, D., Marziani, P., & Sulentic, J. W. 2012, ApJ, 757, 62
Negrete, C. A., Dultzin, D., Marziani, P., & Sulentic, J. W. 2013, ApJ, 771, 31
Netzer, H. 2013, in The Physics and Evolution of Active Galactic Nucleied. H. Netzer (Cambridge: Cambridge Univ. Press), 2013
Netzer, H., & Marziani, P. 2010, ApJ, 724, 318
Osterbrock, D. E., & Ferland, G. J. 2006, in Astrophysics of Gaseous Nebulae and Active Galactic Nuclei ed. D. E. Osterbrock, & G. J. Ferland (2nd ed.; Sausalito, CA: Univ. Science Books), 2006
Persson, S. E. 1988, ApJ, 330, 751
Pickles, A. J. 1998, PASP, 110, 863
Press, W. H., Teukolsky, S. A., Vetterling, W. T., & Flannery, B. P. 1995, Numerical recipes in Fortran: the art of scientific computing (2nd ed.; Cambridge: Cambridge Univ. Press)
Peterson, B. M., & Wandel, A. 1999, ApJL, 521, L95
Punsly, B., & Zhang, S. 2010, ApJ, 725, 1928
Ranade, A., Gupta, R., Ashok, N. M., & Singh, H. P. 2004, BASI, 32, 311
Ranade, A. C., Singh, H. P., Gupta, R., & Ashok, N. M. 2007, arXiv:0705.4560
Rayner, J. T., Cushing, M. C., & Vacca, W. D. 2009, ApJS, 185, 289
Richards, G. T., Kruczek, N. E., Gallagher, S. C., et al. 2011, AJ, 141, 167
Rodríguez-Ardila, A., Viegas, S. M., Pastoriza, M. G., & Prato, L. 2002a, ApJ, 565, 140
Rodríguez-Ardila, A., Viegas, S. M., Pastoriza, M. G., Prato, L., & Donzelli, C. J. 2002b, ApJ, 572, 94
Rudy, R. J., Mazuk, S., Puetter, R. C., & Hamann, F. 2000, ApJ, 539, 166
Sameshima, H., Kawara, K., Matsuoka, Y., et al. 2011, MNRAS, 410, 1018
Sánchez, S. F., Jahnke, K., Wisotzki, L., et al. 2004, ApJ, 614, 586
Sánchez-Blázquez, P., Gorgas, J., Cardiel, N., & González, J. J. 2006a, A&A, 457, 787
Sánchez-Blázquez, P., Gorgas, J., Cardiel, N., & González, J. J. 2006b, A&A, 457, 809
Sánchez-Blázquez, P., Gorgas, J., & Cardiel, N. 2006c, A&A, 457, 823
Sani, E., Lutz, D., Risaliti, G., et al. 2010, MNRAS, 403, 1246
Schlegel, D. J., Finkbeiner, D. P., & Davis, M. 1998, ApJ, 500, 525
Shapovalova, A. I., Popović, L. Č., Burenkov, A. N., et al. 2012, ApJS, 202, 10
Shin, J., Woo, J.-H., Nagao, T., & Kim, S. C. 2013, ApJ, 763, 58
Sigut, T. A. A., & Pradhan, A. K. 1998, ApJL, 499, L139
Sigut, T. A. A., & Pradhan, A. K. 2003, ApJS, 145, 15
Sigut, T. A. A., Pradhan, A. K., & Nahar, S. N. 2004, ApJ, 611, 81
Snedden, S. A., & Gaskell, C. M. 2007, ApJ, 669, 126
Spolaor, M., Proctor, R. N., Forbes, D. A., & Couch, W. J. 2009, ApJL, 691, L138
Sulentic, J. W., Bachev, R., Marziani, P., Negrete, C. A., & Dultzin, D. 2007, ApJ, 666, 757
Sulentic, J. W., Marziani, P., del Olmo, A., & Plauchu-Frayn, I. 2014, A&A, 570, A96
Sulentic, J. W., Marziani, P., & Dultzin-Hacyan, D. 2000a, ARA&A, 38, 521
Sulentic, J. W., Marziani, P., Zamanov, R., et al. 2002, ApJL, 566, L71
Sulentic, J. W., Marziani, P., Zamfir, S., & Meadows, Z. A. 2012, ApJL, 752, L7
Sulentic, J. W., Repetto, P., Stirpe, G. M., et al. 2006, A&A, 456, 929
Sulentic, J. W., Stirpe, G. M., Marziani, P., et al. 2004, A&A, 423, 121
Sulentic, J. W., Zwitter, T., Marziani, P., & Dultzin-Hacyan, D. 2000b, ApJL, 536, L5
Trager, S. C., Faber, S. M., Worthey, G., & González, J. J. 2000, AJ, 120, 165
van Dokkum, P. G., & Conroy, C. 2012, ApJ, 760, 70
Verner, E. M., Verner, D. A., Korista, K. T., et al. 1999, ApJS, 120, 101
Verner, E., Bruhweiler, F., Verner, D., Johansson, S., & Gull, T. 2003, ApJL, 592, L59
Véron-Cetty, M.-P., Véron, P., & Gonçlves, A. C. 2001, A&A, 372, 730
Wang, H., Wang, T., Zhou, H., et al. 2011, ApJ, 738, 85
Wilcoxon, F. 1945, Biometrics Bull, 1, 80
Wills, B. J., Netzer, H., & Wills, D. 1985, ApJ, 288, 94
Wyse, R. F. G., & Gilmore, G. 1988, AJ, 95, 1404
Zamfir, S., Sulentic, J. W., Marziani, P., & Dultzin, D. 2010, MNRAS, 403, 1759